



HAL
open science

Characterization of Eu doped ZnO micropods prepared by chemical bath deposition on p-Si substrate

Nouf Ahmed Althumairi, Irshad Baig, Tarek Said Kayed, Abdelkarim Mekki, Alain Lusso, Vincent Sallet, Abdul Majid, Afif Fouzri

► **To cite this version:**

Nouf Ahmed Althumairi, Irshad Baig, Tarek Said Kayed, Abdelkarim Mekki, Alain Lusso, et al.. Characterization of Eu doped ZnO micropods prepared by chemical bath deposition on p-Si substrate. Vacuum, 2022, 198, pp.110874. 10.1016/j.vacuum.2022.110874 . hal-03738402

HAL Id: hal-03738402

<https://hal.science/hal-03738402>

Submitted on 26 Jul 2022

HAL is a multi-disciplinary open access archive for the deposit and dissemination of scientific research documents, whether they are published or not. The documents may come from teaching and research institutions in France or abroad, or from public or private research centers.

L'archive ouverte pluridisciplinaire **HAL**, est destinée au dépôt et à la diffusion de documents scientifiques de niveau recherche, publiés ou non, émanant des établissements d'enseignement et de recherche français ou étrangers, des laboratoires publics ou privés.

Characterization of Eu doped ZnO micropods prepared by Chemical Bath Deposition on p-Si substrate.

Nouf Ahmed Althumairi^{1,2,3}, Irshad Baig², Tarek Said Kayed⁴, Abdelkarim Mekki^{5,6}, Alain Lussou⁷, Vincent Sallet⁷, Abdul Majid⁸, Afif Fouzri^{1,2,*}

¹Department of physics, College of Science, Imam Abdulrahman Bin Faisal University, P.O. Box 1982, Dammam 31441, Saudi Arabia.

²Basic & Applied Scientific Research Center, Imam Abdulrahman Bin Faisal University, P.O. Box 1982, Dammam 31441, Saudi Arabia.

³Department of Biology, College of Education, Majmaah University, P.O. Box 66, Almajmaah 11952, Saudi Arabia.

⁴Department of Basic Engineering Sciences, College of Engineering, Imam Abdulrahman Bin Faisal University, P.O. Box 1982, Dammam 31441, Saudi Arabia.

⁵Department of Physics, King Fahd University of Petroleum & Minerals, Dhahran 31261, Saudi Arabia.

⁶Interdisciplinary Research Center for Advanced Materials, King Fahd University of Petroleum & Minerals, Dhahran 31261, Saudi Arabia.

⁷Groupe d'Etude de la Matière Condensée (GEMAC), CNRS, Université de Versailles-St Quentin en Yvelines, Université Paris-Saclay, 45 Avenue des Etats-Unis, 78035 Versailles, France.

⁸Department of Physics, College of Science, Zulfi 11932, Majmaah University.

* Corresponding author (email: Anfouzri@iau.edu.sa)

Abstract:

The chemical bath deposition method was used to synthesize Eu-doped ZnO on p-type (100) silicon. The SEM image shows the formation of micropod-like ZnO. EDX and XPS measurements showed an increase in the Eu concentration up to 2.54% and the simultaneous presence of Eu³⁺ and Eu²⁺. XRD analysis confirmed that the interstitial Eu³⁺ ions distorted the

four tetrahedral bonds, and the substitution of Eu^{2+} ions increased the c lattice parameter. Only $\text{Eu}^{3+} \ ^5\text{D}_0 \rightarrow \ ^7\text{F}_2$ transition-related emission was observed, so a weak transfer energy from the ZnO matrix to the Eu ion occurred. However, the competition between the emission of deep-level defects in the host matrix and that of Eu^{3+} ions deforms the visible emission towards the red color. The I-V measurements of the Eu-ZnO/p-Si heterojunctions showed diode-like behavior with a low rectification ratio and a barrier height around 0.84 eV not affected by the Eu concentration.

1. Introduction

Zinc oxide (ZnO) is a very promising material in the field of optoelectronic materials and their applications, particularly in lighting technology. It has a wide band gap 3.37 eV and a large exciton binding energy (60 meV) [1] at room temperature, which prevents them from absorbing photons with an energy lower than this gap, making them transparent to visible light. This type of material has attracted great interest in recent years owing to its remarkable optical and electrical properties. Indeed, it can offer a very good compromise between their optical transparency in the visible region (transmission greater than 80%) and their electrical conductivity (up to 10^{-4} Ω cm), which make them excellent candidates for applications in optoelectronics (light-emitting diodes LEDs) [2], photovoltaics (transparent electrodes in solar cells or in transparent electrical contacts), or even in electrochromic windows [3]. ZnO is an intrinsically n-type semiconductor. Its p-type doping remains controversial, and the p-n homojunctions are far from being well mastered. For this, the growth of ZnO on other p- and n-type materials, such as Si and GaN, continues to receive much attention. The potential applications of ZnO-based films in electronic devices in the form of heterostructures such as ZnO/Si require a deep understanding of the properties and mechanisms of transport across these heterojunctions. Good quality heterojunctions and devices (LEDs) can be produced. The ZnO/Si heterostructure is one of the most important structures studied because silicon is the most widely used. Doping and co-doping ZnO is a very effective way to improve its physical properties [4]. Doping is a suitable method to improve and control the electrical, optical, and other material properties of ZnO, which is crucial for its useful applications. Doping drastically changes the properties of a material without changing its crystal structure. ZnO is a suitable host material for various dopants. It is well established that the luminescence of ZnO at room temperature has two emission bands. One in the ultraviolet (UV) region is attributed to the typical band edge transition or combination of excitons, and the other is quite broad in the visible region from 400 nm to 700 nm [5], which is recognized as the defect emission. In fact, these defect states located between the valence and conduction bands cause luminescence in the visible range. In general, the spectral range of blue/green (400-500 nm) is due to states arising from zinc defects, whether interstitial (Zn_i) or lacunar (V_{Zn}) and the green/red domain (500-800 nm) is associated with defects involving oxygen [6,7]. However, their intensities and chromaticities are not sufficient to exploit them in applications that use precise colors [6]. As our eyes are more sensitive to monochromatic colors than to those of the broad band spectrum, doping ZnO with rare earth (RE) ions may therefore be an

appropriate method to overcome this disadvantage. In fact, rare earth ions (RE^{3+}) are emitted in the visible-IR spectral region, resulting in stable and multiple sharp bands at a single excitation. Thus, doping ZnO with rare-earth ions makes it possible to obtain the luminescence of these added to that of the matrix. The superposition of the main optical transition for RE allows the control of the color emitted by the material, which requires an efficient direct energy transfer from ZnO to the RE element. However, the difference in ionic radii with that of Zn, which is not negligible, induces a low solubility of rare earth in the matrix [7] and may lead to ineffective and/or reduced energy transfer. The choice of Eu^{3+} ions for ZnO doping can produce either red-or orange-emitting materials in the near-ultraviolet (UV)/blue region, which is useful for developing white LED applications or for performing optoelectronic devices with red emission. Studies of Eu^{3+} -doped ZnO have been explored by many authors [8,9] who observed an efficient red emission, confirming the incorporation of Eu ions into the ZnO host [10,11]. However, different results regarding the efficiency of the energy transfer mechanisms from ZnO to RE ions have been obtained. Several energy transfers from the ZnO host to RE ion models have been proposed [12-14]. There are those who assume a mediated process of defect levels [12] and others assume the formation of a bound exciton after trapping free carriers by the RE-bound levels, which excites the 4f core levels [13,14]. In another model, the recombination of free excitons results in UV emission and/or transfers energy to RE ions [13]. It is well known that the red emission of Eu^{3+} occurs from the ${}^5D_0-{}^7F_2$ transition, which is affected by the surrounding atoms inside the ZnO matrix [15]. On the other hand, the coexistence of the divalent and trivalent oxidation states of Eu in the ZnO host [16] could inevitably generate and/or disturb defect energy levels in the band gap of ZnO, which could strengthen or weaken the energy transfer mechanism from ZnO to Eu centers, thereby improving the color emission quality of the sample. Today, ZnO micro- and nanostructures can be produced with a wide variety of morphologies. In addition to the planar structure of micro/nanometric thickness, micropods, nanorods, nanotubes, nanoflowers, and twin structures have been prepared using different growth methods [17]. It is also possible to influence the PI properties by doping impurities in the ZnO morphology [18]. In fact, an enhancement in radiative recombination is observed in the case of single-dimensional ZnO, which is a consequence of quantum confinement [18]. In this work, Eu-doped ZnO micropods were synthesized by the chemical bath deposition (CBD) method, deposited on p-Si (001) substrates, and annealed at different temperatures for 2 h. Apart from being a low-temperature process, CBD is used for simple experimental setups and possible growth on a variety of substrates on a large scale. It is a cheap and convenient technique for

the commercial production of ZnO-based devices. The structural, morphological, electrical, and optical properties of Eu-doped ZnO were studied as a function of the Eu concentration and annealing temperature. Their color emission and color-correlated temperature (CCT) were also investigated based on the CIE chromaticity coordinates. The possible presence and efficiency of energy transfer between the ZnO host and Eu³⁺ ion levels are also discussed.

2. Experimental details

2.1. Samples preparation

Pure ZnO and Eu-doped ZnO were synthesized using the chemical bath deposition (CBD) method on p-Si (001) substrates. For preparing the solution, 0.05M Zinc acetate dehydrate ($\text{Zn}(\text{CH}_3\text{CO}_2)_2 \cdot 2\text{H}_2\text{O}$) (Chem-Impex, 99.18%) was dissolved in 250 ml of deionized water (18 M Ω cm). Then, 1 ml of ammonium hydroxide (NH_4OH) (Sigma-Aldrich) was added to this solution and stirred at room temperature. Growth was performed in the absence of metal catalysts or additives. This solution was then heated to 87°C using a hot-plate magnetic stirrer. ZnO microstructures form freely in the solution and can therefore be deposited on any substrate. This preparation procedure and possible chemical pathway for the growth of ZnO microstructures have been previously reported in recent published works [17,19,20]. Bore-doped p-type (100) silicon substrates with a resistivity of 1-10 Ω cm and a thickness of 525 μm were used to deposit the microstructures. The cleaned substrate, fixed with straight forceps, was placed vertically in the prepared solution once the temperature of the solution reached 87°C for a period of 4 h. Thereafter, the samples were washed with deionized water and dried using an air gun. The synthesis of Eu-doped ZnO was performed similarly; however, different weight percentages of Europium III nitrate pentahydrate ($\text{Eu}(\text{NO}_3)_3 \cdot 5\text{H}_2\text{O}$) (American Elements, 99.9%) to the zinc acetate precursor, to obtain different concentrations of dopant. The chosen weight ratios (wt %) of Eu/Zn in the prepared solutions were 5%, 10%, 15%, and 20%.

2.2 Annealing of the samples

Our samples were annealed at $T_a=300, 500, \text{ and } 700$ °C in an air atmosphere for a time period of 2 h, and their physical properties were compared to those of the grown sample.

2.3. Samples Characterization

Scanning Electron Microscope & EDX (A VEGA 3 TESCAN scanning electron microscope Tescan) is equipped with a detector of secondary electron (SE), and an X-ray detector alongside with an electron backscatter diffraction (EBSD) system which are respectively employed for “in situ” diffraction mapping, chemical composition analysis and morphology

observation. Material analysis was carried out at a voltage of 15 keV with a working distance of 10 mm between the specimen and the detector without any polishing or conductive coating. The compositional characterization of our samples was performed using EDX (mapping well as spectra at four different positions). The chemical composition of the samples and the oxidation states of the elements were evaluated by X-ray photoelectron spectroscopy (XPS) using a Thermo Scientific Escalab 250 Xi XPS spectrometer. The energy resolution was ~ 0.5 eV. Monochromatic Al K_{α} X-rays were used to irradiate the samples. A flood gun was used to neutralize the charging effects. Ar^+ ion bombardment of the samples was performed in an XPS UHV chamber by applying an acceleration potential of 3 kV for 30 s. A survey scan was performed to assess all the elements present. The Zn 2p, O 1s, Eu 3d, and C 1s high-resolution XPS spectra were acquired. The base pressure in the chamber was originally 1×10^{-10} mbar. However, during ion bombardment, the pressure was $\sim 1 \times 10^{-9}$ mbar. The energy scale was calibrated using the binding energy of carbon C 1s peak at $(289.58 - \phi_{\text{ZnO}})$ eV [21] where $\phi_{\text{ZnO}} = 4.85$ eV is the undoped ZnO work function reported by Lee et al. [22]. Experiments were repeated to verify the reproducibility of the results. The dedicated software “Avantage” was used to fit the experimental data. The optical properties of the samples at room temperature were investigated by UV-visible spectrophotometry using a Shimadzu SolidSpec-3700DUV and photoluminescence (PL) experiments. Two laser sources were used in the study. A 325 nm (3.82 eV) He-Cd laser and a 405 nm (3.06 eV) diode laser. Therefore, it is possible to observe the energy transfers between the ZnO matrix and the dopant and those between the deep-level defects and dopant. The current-voltage (I-V) measurements of our elaborated samples were carried out by adapting the voltammetric techniques (in our case, linear sweep voltammetry) in Palmsens4 instruments usually used for electrochemical applications.

3. Results and discussions

3.1. Europium incorporation

To determine the composition of elements and their distribution in the ZnO matrix, EDX mapping and spectra were carried out for all samples. The atomic percentage of Eu present in our samples Y wt % Eu-ZnO (where Y represents the Eu weight percentage used in the preparation of the CBD solution) was determined based on the atom concentration measured by EDX at three positions and in a small selected area. The Eu concentration (X_{Eu}) incorporated in the ZnO lattice was determined using the $\text{Eu}/(\text{Eu} + \text{Zn})$ ratio [23]. The average values are listed in Table 1 and were considered in our work. EDX results show that Eu

incorporated in the doped ZnO samples not exceed 2.5% although a 20% weigh percentage of Europium III nitrate pentahydrate ($\text{Eu}(\text{NO}_3)_3 \cdot 5\text{H}_2\text{O}$) was used in the preparation of the CBD solution. Therefore, the greatest amount of dopant was precipitated at the bottom of the CBD solution beaker. This means that low-temperature CBD synthesis is not a good method for doped ZnO with a high Eu concentration, even if the samples are annealed after growth. Within the ZnO matrix, the Eu can be located at various sites. However, only two positions appear to be acceptable from an energy perspective. First, the Eu can be placed on an interstitial site (Eu_i) or replace the Zn^{2+} ion (Eu_{Zn}). The stabilization of the Eu in either case position requires some energy of formation, E_f . The energies calculated by the numerical method are given for each position (Eu_i and Eu_{Zn}) 1,429 and -2,391 eV, respectively. As a result, substitute Eu is more favorable than interstitial Eu [23]. When these ions are located on coordination site 4, the ionic radii of Zn^{2+} , Eu^{3+} , and Eu^{2+} are 60, 90, and 110 pm, respectively [15]. At first glance, the difference in ionic radii is not negligible, which induces low solubility (a few percent) of Eu in the matrix [24]. Despite this low solubility, diffusion of Eu ions from the surface of the sample into the volume [25] can occur when the sample is annealed. As seen in Table 1, the increase in X_{Eu} with the annealing temperature is probably caused by the diffusion of dopant ions. EDX and element overlap maps were performed on a $5\mu\text{m} \times 5\mu\text{m}$ area of the sample surface. The EDX maps for all samples are similar, so we show as an example that the 5 wt % Eu-doped ZnO sample as grown ($X_{\text{Eu}}=1.00\%$) and that of 20 wt % Eu-doped ZnO annealed at 700 C ($X_{\text{Eu}}=2.54\%$) in Figure 1 (a) and (b), respectively.

EDX maps show the presence of Si, Zn, O and Eu elements for all samples. However, the coverage of the substrate by the ZnO microstructure differs from region to region and from sample to other. Europium EDX maps show a distribution across the surface of the sample with an atomic percentage that is not perfectly uniform.

3.2. Sample morphology

The sample morphologies of all samples were examined using SEM, and the images of the as-grown and heated at 300, 500, and 700 C of undoped and Eu-doped ZnO are shown in Figure 2. Different micropod shapes can be clearly observed, with the majority having two arms (bipods). However, we can also see micropod cross-linked structures with many arms. These micropods are distributed over a silicon substrate with different dimensions that can reach 1.7 μm length and diameter of 1 μm . Most micropods have a hexagonal shape with very smooth sidewalls. By looking more closely, we can see the presence of obscure tasks in these arms when the sample is heated at temperatures higher than 500C. As the heat temperature is high, these tasks are clearer and larger owing to the formation of structural defects at the ZnO

micropod surface, which originate from the evaporation of the precursor elements in the solution followed by recrystallization inside the micropods [19] during the annealing treatment. A possible growth mechanism of these multipods has been reported by Gokarna et al. [19]. Once the solution is supersaturated, initial nucleation begins and over time leads to the formation of ZnO microstructures in the solution, as reported by Cao et al. [26] for ZnO nanorods and nanoplates. When the solution is heated, Zn^{2+} ions react directly with OH^- ions to form ZnO by aggregation of nanoparticles along the c-axis of the hexagonal crystal, leading to organized growth of ZnO micropods [20,27]. These micropods thus generated precipitates in the aqueous solution and could grow on a common junction, keeping the growth along their hexagonal c axes of the individual crystals generating several arms, as reported by Majitha et al. [27]. As the growth is free in the solution, the number of arms in these twin structures cannot be controlled.

3.3 Chemical analysis

X-ray photoemission spectroscopy (XPS) analyses were carried out for the undoped and 20 wt % Eu-doped ZnO micropods grown on Si substrates and annealed at 300, 500 and 700C to analyze the oxidation state and presence of atoms at different positions (substitution and/or interstitial). Figure 3 shows the XPS high-resolution spectra for the Zn2p, O1s and Eu3d core levels. The wide-scan XPS survey spectra are also provided. The binding energy scale was calibrated using the C 1s peak at 284.73 eV. This is due to surface contamination during sample exposure to ambient atmosphere. All peaks within the survey spectra (Figure 3) were assigned, according to the XPS handbook [28], to the core levels of Zn, Si, O, C, and Eu with no impurity. The XPS spectra for the Zn2p core level show two peaks centered at around 1021.93 and 1044.93 eV corresponding to $Zn^{2+}2p_{3/2}$ and $Zn^{2+}2p_{1/2}$, respectively, which are very close to those reported in the literature (1021.9 and 1045.4 eV) [29]. The presence of these two intense peaks confirms the hexagonal wurtzite structure of the ZnO micropods [8,30]. The energy difference between the two peaks is 23 eV, very close to the standard value (22.97 eV) confirming the existence of Zn^{2+} ions [31]. In Figure 4. we have plotted the XPS binding energy spectra for the Zn2p core level of undoped and 20 wt % Eu-doped ZnO treated at the same temperature. A small shift to high energy was observed as the temperature of the annealing micropods increased, which was due to the increase in structural defects, as seen in the SEM images. A shift to lower energy appears for 20 wt %Eu-doped ZnO, probably because of an inverse competition between the appearance of structural defects generated by the increase in the annealing temperature and those caused by the incorporation of the Eu into the ZnO matrix. The shift and the reduction in peak intensity as a function of annealing

temperature can be attributed to the presence of excess Zn in the undoped sample and/or a transfer of electrons between dopants and Zn in the doped sample that occur via the structural defects [30,32]. The shape of the XPS spectra of the O 1s peak (Figure 3) suggests the presence of more than one component. Each individual component was extracted by fitting the peak with a multiple Gaussian. The deconvolution of the O 1s XPS core level peak for the undoped and 20 wt % Eu-doped ZnO micropods grown on the Si substrate and annealed at 300, 500 and 700C are represented in Figure 5. The O 1s of the undoped ZnO micropods could be fitted by three components centered at approximately 529.63, 530.73 and 532.48 eV. However, the O 1s peak of the 20 wt % Eu-doped ZnO was deconvoluted into four components centered at approximately 526.03, 530.13, 531.73, and 532.33 eV (Figure 5). The peak labeled O₁ in Figure 5 is assigned to O²⁻ ions in the hexagonal wurtzite structure of ZnO, forming bonds with Zn²⁺ ions (O-Zn groups) [32]. The O₂ peaks are related to O²⁻ ions residing in the oxygen-deficient region within the ZnO lattice (O-deficient groups). The higher binding energy peak (O₃) at approximately 532.33 eV is usually correlated with surface-adsorbed oxygen species such as CO₂ and adsorbed H₂O (O-H groups). These three oxygen chemical states are consistent with the values reported in the literature [8,32]. However, in our case, we observed another weak and broad peak located around 526.03 eV which can be attributed to the H-ZnO (10-10) surface. In fact Kotsis and Staemmler using ab initio calculation, report that the binding energy of oxygen from H-ZnO (10-10) surface is lower than that of the oxygen in bulk ZnO [33]. The peak position and area ratio of the three peaks O₁, O₂, and O₃ (corresponding to O-Zn, O-deficient groups, and O-H groups) at different annealing temperatures are listed in Table 2. As the annealing temperature of the undoped ZnO micropods increased, a shift similar to that observed for the Zn2p XPS core level peak was observed with a decrease in the area ratio of the O-deficient groups and an increase in the O-Zn and O-H groups. The O-H group area ratio was higher than that of the O-deficient groups when the annealing temperature exceeds 500C (Table 2). The area ratio of the O-Zn and O-H groups varied inversely compared to that of the O-deficient groups. They exhibit small variations when the ZnO micropods are annealed at temperatures ≤ 300°C, whereas O-deficient groups dominate at low temperatures. When the annealing temperature exceeded 300°C, the O-Zn and O-H groups began to increase significantly in the same time O-deficient groups decreased. That is, the free oxygen atoms coming from outside the wurtzite structure filled more oxygen vacancies during high-temperature heating. In fact, Jiang et al. [34] reported the same effect for zinc oxide thin-film transistors and explained the ease of penetration of oxygen atoms into atomic spaces by enlarging the atomic spaces of the

wurtzite structure or increasing the dynamic energy of the atoms at high temperatures. During cooling, these oxygen vacancies are filled; during cooling, they are transformed into O-Zn groups. A higher concentration of oxygen vacancies generally induces a higher concentration of carriers, which would be beneficial for the electrical performance of our heterojunctions. Therefore, the heterojunction annealed at temperatures ≤ 300 °C proved to be more electrically efficient. For 20 wt % Eu-doped ZnO, the intensity of the O-H groups (O_3 peak) decreased with the increase in annealing temperature, but increased again at 700 C. The O-Zn and O-deficient groups (O_1 and O_2 peaks, respectively) show an inverse variation tendency as the annealing temperature increases up to 500C. The O-Zn group increased at the same time as the O-deficient and O-H groups decreased. This can be explained by filling some oxygen vacancies with free oxygen or Eu atoms as the annealing temperature increased. However, for the sample annealed at 700 C, the intensity of the deficient peak re-increase may be due to the appearance of more structural defects in the ZnO micropods, as confirmed by scanning electron microscopy. A small shift was observed when we compared the XPS binding energy spectra for the O 1s core level of undoped and 20 wt % Eu-doped ZnO heated at the same temperature (Figure 6). For $T_a \leq 300$ C, this shift is towards a high binding energy, but it inverts toward a lower binding energy for 20 wt % Eu-doped ZnO heated at $T_a \geq 500$ C. The same reason given previously for the Zn2p peak can also explain this shift inversion. The area ratio variation of the deconvoluted O 1s peak as a function of heat treatment and Eu incorporation will influence the luminescence properties of our samples, as reported by Kumar et al. [35,36]. Four peaks appeared in the XPS spectra of the Eu 3d level for the 20 wt % Eu-doped ZnO (Figure 3) at around 1125.63 eV, 1134.83 eV, 1155.33 eV and 1164.63 eV for the different T_a . The peaks obtained at 1134.83 eV and 1164.63 eV are assigned to the Eu $3d_{5/2}$ and $3d_{3/2}$ respectively. The 29.8 eV binding energy difference matches the values corresponding to Eu^{3+} ions (trivalent state) in the ZnO matrix, as reported in many previous works [16,32]. This difference is characteristic of charge transfer between the energy levels of O 2p and Eu 4f [37]. The other two peaks distinguished at the lower binding energy side of Eu^{3+} correspond to the Eu^{2+} ions (divalent state) $3d_{5/2}$ and $3d_{3/2}$ core levels [11,32]. Trivalent and divalent ions result from $3d 4f^6$ and $3d 4f^7$ configurations [11]. This confirms the coexistence of divalent and trivalent oxidation states of Eu in the doped sample [16]. It is likely that the Eu^{2+} substituted Zn^{2+} ions in ZnO lattice. As the X-ray diffraction measurements (discussed in the next section) do not provide evidence for the presence of europium oxide (Eu_2O_3), Eu^{3+} can be found on the surface of the microprods and/or Si substrate and can also occupy an interstitial site (Eu_i) or lock onto the grain boundaries [38].

To assess dopant concentration, $C_x(\%)$, the spectral areas of Zn and dopant ions were calculated using the following formula:

$$C_x = \frac{(A_x/S_x)}{\left(\sum_i A_x/S_x\right)}, \quad (1)$$

where A_x and S_x represent the XPS spectral area and the sensitivity factor (RSF) of the element, respectively. The denominator denotes the sum of the ratios of the XPS spectral area to the sensitive factor of all the elements in the sample. When preparing the CBD solution for the doped sample, the weight percentage of Eu/Zn was fixed. To compare the dopant concentration estimated by XPS measurement to that obtained by EDAX, Eu_i ($i=+2$ or $3+$) was calculated from the XPS curves using the following equation:

$$C_{Eu^i} = \frac{(A_{Eu^i}/S_{Eu})}{(A_{Eu^{2+}}/S_{Eu}) + (A_{Eu^{3+}}/S_{Eu}) + (A_{Zn^{2+}}/S_{Zn})}, \quad (2)$$

The sensitivity factors were obtained from the library available using the instrument fitting software (Avantage). Table 3 lists the values used and the calculated Eu^{2+} and Eu^{3+} concentrations obtained via XPS experiments for the 20 wt % Eu-doped ZnO micropods. In the XPS technique, X-rays are sent to the sample, and ejected electrons are detected. However, in EDX, electrons are sent to the sample, and the generated X-ray photons are detected. Although the sample composition can be obtained using both techniques, the main XPS signal comes from the surface (a few atomic layers at the surface, so a few nanometers because only those electrons generated near the surface escape from the sample surface and are detected. The depth of the incident beam when measuring the EDX (approximately 1 μm) was much greater. In addition to the non-uniformity of the substrate coverage by the micropods, the analysis volume when measuring XPS and EDX is different, which gives rise to the difference in the obtained Eu concentration. The estimated value by EDAX represent rather the "bulk" concentration in a sample but XPS one gives the near surface region chemical composition. The Eu^{2+} and Eu^{3+} concentrations did not vary monotonically as the annealing temperature increased. It is possible that the Eu^{3+} ions at the surface of the ZnO micropods migrate deeper into the volume and replace the Zn^{2+} ion or inversely.

3.4 Structure analysis

The crystal structures of the synthesized Eu-doped ZnO micropods with different Eu concentrations on the Si substrate as grown and annealed at 300, 500 and 700C were analyzed using XRD measurements. Figure 7 (a-d) show the corresponding patterns. For each sample,

XRD measurements were performed after alignment of the diffractometer on the (002) Si peak. The X-ray spectra of all samples show a superposition of the ZnO micropods and substrate peaks. The Miller indices of the planes are labeled at higher for each peaks in the XRD pattern. The peaks observed at 32.94° correspond to the diffraction from the (002) plane of the Si substrate. The micropod peaks corresponding to the diffraction from Bragg's planes (100), (002), (101), (102), and (110), respectively, are attributed to the wurtzite hexagonal structure. These XRD peaks match the values of the standard card for zincite ZnO (JCPDS No. 36-1451). Comparing the XRD patterns of the undoped samples, a slight shift in the peak positions was observed with increasing Eu concentration. We also noted remarkable variations in the intensities of the various peaks of the micropods compared to those in the standard card for zincite ZnO, and as the Eu doping concentration increased. Several factors, including shape, orientation, and strain, influence the broadening, intensity, and position of the diffraction peaks. In fact, a possible relative intensity variation in the XRD spectra can occur according to the direction and degree of particle alignment. A recent paper [39] that treats the key aspects of powder X-ray diffraction data to analyze nanoscale material samples. In fact, a sample of non-spherical particles growing in a solution tends to orient with their flat faces, corners, or edges parallel to the deposition substrate. Consequently, preferential orientation of the particles according to a particular crystallographic direction of the material lattice can be manifested [39]. Depending on the quality and size of the different forms of particles, the majority of the sample or only a fraction will exhibit a preferred orientation in the X-ray spectrum. The morphology obtained for our sample and their random distribution on the surface of the silicon substrate affect the relative intensities of the peaks in the XRD data; however, their position 2θ for the undoped sample matched well with the reported XRD ZnO spectra in the literature. The preferential orientations were quantified by defining the crystallite orientation parameter. This parameter can be calculated using the following equation [40]:

$$P_{(hkl)} = \frac{I(hkl)}{I(100) + I(101) + I(002)}, \quad (3)$$

where $p_{(hkl)}$ is the ratio of the measured intensity of the (hkl) planes by the sum of the three first and high-intensity peaks. Table 4 regrouped these values for our samples as a function of the annealing temperature T_a . The $p_{(hkl)}$ of commercial ZnO powder (Sigma-Aldrich inventory: 1314-13-2), calculated from the XRD spectrum measured under the same conditions, is also shown for comparison. The values of the orientation parameter obtained for

our micropods show a preferential orientation along the axis [100], which is different from that of the powder ([101]), thin film [40,41], and nanorods ([002]) [42]. As the micropods grow along the c-axis of the wurtzite structure, perpendicular to the [100] direction, most of the deposited ZnO micropods are longitudinally on the surface of the silicon substrate (micropods tend to orient flat on a substrate upon drying) and the other is randomly oriented, which explains the low intensity of other X-ray peaks. This arrangement of micropods can be explained by the small lattice mismatch between the substrate ($a = 5.43 \text{ \AA}$) and ZnO ($c = 5.20 \text{ \AA}$). The lattice parameters 'a' and 'c' for doped ZnO micropods deposited on p-Si substrates are calculated and listed in Table 3 by using the following equation [41]:

$$d_{hkl} = \left(\frac{4}{3} \frac{h^2 + h.k + k^2}{a^2} + \frac{\ell^2}{c^2} \right)^{-1/2}, \quad (4)$$

Where d_{hkl} is the interplanar spacing. The experimental errors in the lattice parameters were estimated to be 0.003 \AA . The c/a ratio and cell volume are also given in Table 3 as functions of the Eu concentration. To study the evolution of lattice distortion, the nearest-neighbor bond lengths along the c-direction (expressed as b) and off c-axis (expressed as b_1) are calculated as [43]:

$$b = cu \text{ and } b_1 = \sqrt{\frac{1}{3}a^2 + \left(\frac{1}{2} - u\right)^2 c^2}, \quad (5)$$

Where u is the internal parameter equal to $3/8=0.375$ (in an ideal wurtzite structure) and is defined as the nearest-neighbor distance parallel to the c-axis divided by the c lattice parameter. The u parameter is related to the c/a ratio ($=1.633$ in an ideal wurtzite structure) as follows [43]:

$$u = \left(\frac{1}{3}\right)\left(\frac{a}{c}\right)^2 + \frac{1}{4}, \quad (6)$$

The u parameter and bond length b , b_1 of Eu-ZnO micropods on p-Si substrate as a function of Eu concentration are regrouped in Table 5 for the different annealing temperatures. The lattice parameter for ZnO micropods is slightly lower than that given by JCPDS card 36-1451 and those of commercial ZnO powder, probably due to the strain, which is higher than that of ZnO powder. The a-and c-lattice constants and bond lengths b and b_1 are plotted as functions of the Eu concentration for different T_a values in Figures 8 (a) and (b), respectively. By inspecting the different structural parameters of our samples as a function of the annealing temperature and Eu concentration incorporated in ZnO micropods, we observe that their variations are not monotonous, but the ratio (c/a) and the internal structural parameter u are

practically unchanged. Their values are in good agreement with those determined by theoretical calculations and various experimental techniques [1]. So the wurtzite structure of our micropods remains stable. The variations in the structural parameters of the undoped sample are the result of point defects such as zinc antisites, oxygen vacancies, and extended defects, such as threading dislocations and strain, which differ according to T_a . However, for doped micropods, the incorporation of Eu ions also induces such structural modifications as their radii are higher than those of Zn and O. As confirmed by XPS measurements, the Eu can be placed on an interstitial site (Eu_i) or it replaces the Zn^{2+} ion (Eu_{Zn}) (radii=0.74 Å). The compactness of the ZnO structure is approximately 50% [44]. This makes it possible to insert dopants instead of zinc or interstitial sites. The radius of this interstitial site is on the order of 95 pm, which is equal to the ionic radius of Eu^{3+} [44]. Therefore, the location of the doping ion at the interstitial site or in substitution will distort the cell lattice differently. The four tetrahedral bonds undergo a slight variation through a distortion of the tetrahedral angles and a slight change in distance to maintain a strong correlation between the c/a ratio and the parameter u . Similar behaviors have been reported for lattice parameters and bond lengths in high-pressure experiments [45]. The crystallite sizes were calculated using the Debye-Scherrer equation [46]:

$$t_{DS}(hkl) = \frac{k \lambda}{\beta_{hkl} \cos(\theta_{hkl})}, \quad (7)$$

where $t_{DS}(hkl)$ is the crystallite size in the direction perpendicular to the lattice planes (hkl) being analyzed, K is the crystallite-shape factor, λ is the wavelength of the X-rays, β_{hkl} is the full width at half-maximum (FWHM) of the XRD peak, and θ_{hkl} is the Bragg angle. The crystallite size is the average size of the perfectly arranged unit cells, calculated from the FWHM of the XRD peaks. The constant k is taken as 0.9, as reported for nanorods [46]. The axis of the micropods is parallel to the c -axis of the wurtzite structure, so the crystallite size calculated from the FWHM of the (002) peak using the Scherrer equation represents the length of the crystallite forming the micropods. Because the radial direction [110] is orthogonal to the c -axis, the diameter of this crystallite can be assimilated to the crystallite size estimated using the FWHM of the (110) planes. The dislocation (line defects in the regular crystal lattice) density (δ) along the crystallographic plane (hkl) can be calculated using the formula [41]:

$$\delta_{DS}(hkl) = \frac{1}{t_{DS}^2(hkl)}, \quad (8)$$

It represents the amount of defects in the sample along each planes. The calculated crystallite sizes and dislocation density for (002) and (110) peaks are summarized in Table 6. The corresponding values for the commercial powder is also given for comparison. For as grown samples, the estimated crystallite size from the plane (002) are practically unchanged (≈ 40 nm) independently of Eu concentration suggesting no effect of doping on the length of the crystallite forming the micropods. However, the crystallite size calculated from the plane (110) increase with the Eu concentration in ZnO and it reach 65nm for $X_{Eu}=1.88\%$. This behavior is not observed for annealed samples which is due to diffusion of the Eu dopant and the variation of the intrinsic structural defects. To explore the effect of annealing temperature on the structural parameter of un-doped and doped ZnO micropods with the same Eu concentration, lattice parameters and bond length are plotted as function of annealing temperature in Figure 9. For un-doped sample (Figure 9 (a)) lattice parameters and bond length decrease when sample are annealed at 300C for 2 hour and re-increase for 500 and 700C. It represents the amount of defects in the sample along each plane. The calculated crystallite sizes and dislocation densities for the (002) and (110) peaks are summarized in Table 6. The corresponding values for the commercial powder are also provided for comparison. For the grown samples, the estimated crystallite size from the (002) plane is practically unchanged (≈ 40 nm), independent of the Eu concentration, suggesting that doping did not affect the length of the crystallites forming the micropods. However, the crystallite size calculated from the (110) plane increased with the Eu concentration in ZnO and reached 65 nm for $X_{Eu}=1.88\%$. This behavior was not observed for the annealed samples, which was due to the diffusion of the Eu dopant and the variation in the intrinsic structural defects. To explore the effect of annealing temperature on the structural parameters of undoped and doped ZnO micropods with the same Eu concentration, the lattice parameters and bond lengths are plotted as a function of annealing temperature in Figure 9. For the undoped sample (Figure 9 (a)), the lattice parameters and bond length decreased when the sample was annealed at 300C for 2 h and re-increased for 500 and 700C. This is due to an atomic rearrangement during crystallization of ZnO into wurtzite lattice structure engendered by the increase of the thermal energy. This energy seems to help atoms align themselves in the (110) plane, which is manifested by a decrease in the dislocation density along the (110) crystallographic plane with practically no change along the (002) plane. The variation tendency of ZnO micropods doped with practically the same concentration of Eu (Figure 9 (b)) differs for $T_a \leq 500C$. c and b_1 are practically constant, which may be caused by the oxidation of the dopant, so its

localization into the volume of ZnO. In fact, as determined by XPS, the Eu^{2+} and Eu^{3+} concentrations were equal for the samples annealed at 300 and 500C (Table 3). The variations in the structural parameters and bond length as a function of Eu^{2+} and Eu^{3+} for the sample studied by XPS at different annealing temperatures are plotted in Figure 10. The lattice parameters decrease for small (Eu^{3+}) and (Eu^{2+}) concentrations and re-increase at higher concentrations. Therefore, the location of the doping ion at the interstitial site or substitution affects the lattice parameters differently. This is manifested more clearly in the evolution of the bond lengths (Figure 10 (b)). It can be seen that b and b_1 increase monotonically with an increase in the Eu^{2+} (Eu_{Zn}) concentration, which is not the case with the increase in the Eu^{3+} (Eu_i) concentration. We can deduce that the substitution of Zn by Eu^{2+} increases the lattice parameters; however, the interstitial Eu^{3+} in the ZnO matrix causes their change by a distortion of the tetrahedral angles, keeping the wurtzite structure because the c/a ratio and the parameter u are practically invariant.

3.5 UV–vis reflectance analysis

Reflectance spectroscopy measurements on un-doped and Eu doped ZnO/p-Si as grown and annealing respectively 300C, 500C and 700C were conducted in the ultraviolet–visible region (UV–Vis region) from 300 nm to 600 nm. It is a suitable method for the estimation of absorption edges because the silicon band gap is lower than that of zinc oxide. Our samples are thick (thickness $\geq 1 \mu\text{m}$), which prevents accidental loss by partial transmission when measuring the percent reflectance. The detailed optical band gap determination of our samples is described in our recent paper [41]. The corresponding values are listed in Table 7 as function of the X_{Eu} concentration. The band gap of the doped samples was not significantly affected to a great extent by the incorporation of Eu or the annealing temperature. It was observed at 3.22 ± 0.03 eV. This result was reported by Kumar et al. [16] for ZnO:Eu³⁺ nanophosphors. Recent studies have reported that the Eu-doped ZnO band gap decreases, whereas the other band gap increases. Turgut et al. [47] and Kaur et al. [48] reported that it first increased at low Eu concentrations compared to undoped ZnO and decreased at higher concentrations. However, Fonseca et al. [16], Murugadoss et al. [49], and Hasabeldaim et al. [13] reported a continuously decreasing band gap for Eu-doped ZnO nanoparticles which was also obtained by theoretical calculations for other RE dopants [50]. For un-doped and Eu doped ZnO nanorods synthesized by electrochemical-hydrothermal method on FTO coated glass substrates [23], the band gap have been decrease from 3.26 eV to 3.23 eV. Unlike in the reference [51], the optical band gap increases with the Eu doping concentration.

3.6 Photoluminescence study

The photoluminescence (PL) of Eu-doped ZnO micropods as grown and annealed at 300C, 500C and 700C was performed at room temperature and measured at an excitation wavelength of 325 nm using a He-Cd laser. The corresponding spectra are shown in Figure 11. All samples exhibit emission peaks in the ultraviolet (UV) region around 385 nm (3.22 eV) (Table 7) and broad visible emissions, which extend in the range of 450-800 nm. The UV emission peak is attributed to the near-band edge (NBE) emission of ZnO due to excitonic or band-band recombination [52]. The broad visible band is commonly referred to as deep-level emission (DLE) because of the existence of allowed levels inside the band gap induced by the presence of defects in the ZnO structure, which depend on the synthesis technique [52]. A clear vision of the ZnO visible PL mechanism is still far from being fully understood [52]. The position of the UV emission peak for the undoped sample is close to that reported by Guo et al. [53] for ZnO microrods prepared by the float zone method. A weaker emission band is observed at a higher energy of the NBE as a shoulder around 375 nm (~3.306 eV) for doped ZnO micropods annealed at 700C (figure 11 (d) inset). A similar result was reported by Gokarna et al. [19] for undoped ZnO micropods, similarly elaborated but annealed at 900 °C in a nitrogen atmosphere, and can be assigned to the recombination of free excitons (FX_A) [53]. It confirms the good structural quality of our micropods. As the Eu concentration increased, no significant and monotonic variation of the UV peak position was observed; however, it became sharper for the annealed sample and its relative intensity with that of the visible emission band changed significantly. The intensity ratio of the UV peak to visible (I_{UV}/I_{vis}) was higher for the sample annealed at 300C so higher crystallinity [52]. A higher intensity ratio indicates a lower amount of defect sites and better atomic rearrangement during the crystallization of the ZnO micropods. As discussed in the sample morphology section, the presence of residual precursor solution for the unannealed sample and the formation of structural defects after their complete evaporation at 500C can be the origin of the low values of I_{UV}/I_{vis} . The excitation energy (3.82 eV) is beyond the ZnO band gap; therefore, for Eu-doped ZnO, we must obtain the luminescence from the ZnO matrix and from the deep levels within the band gap among them those of the Eu dopant. In fact, the luminescence of the Eu³⁺ ion is characterized by several emission peaks located at the following wavelengths: 579, 591, 616, 649, 690, and 699 nm, corresponding to the transition of $^5D_0 \rightarrow ^7F_i$ ($i=0,1, 2, 3, 4, \text{ and } 5$). The intense emission peak was around 616 nm, and it was only observed for doped micropods as grown around 615 nm. In addition, the substitution of Zn by divalent Eu²⁺, whose energy level is located 0.19 eV below the conduction band [54] can also give an emission around

2.95 eV (420 nm) [54]. As seen in Figure 11, the incorporation of Eu into ZnO micropods induces an asymmetric widening of the visible band with a small shift towards higher wavelengths. The band broadness originates from a superposition of many different ZnO defect emissions and that of the Eu dopant that simultaneously emits. It is clear that the luminescence intensity does not vary monotonically as a function of Eu concentration due to the variation of the defect density with the annealing temperature and/or caused by the larger Eu ions incorporated in ZnO host. Figure 12 displays the room-temperature PL spectra of the Eu-doped ZnO micropods as grown and annealed at 700C when excited using a fiber laser diode at 405 nm. The spectra for as grown sample show peaks at around 579, 591, 615, and 652, characteristic emission of the 4f-4f transitions of the Eu ions. These are attributed respectively to $^5D_0 \rightarrow ^7F_0$, $^5D_0 \rightarrow ^7F_1$, $^5D_0 \rightarrow ^7F_2$, and $^5D_0 \rightarrow ^7F_3$ transitions [14,68]. The broad emission around 696 nm appears to be the result of the overlap of the two transitions $^5D_0 \rightarrow ^7F_4$ and $^5D_0 \rightarrow ^7F_5$. Their emissions depends on the Eu ion symmetry in the ZnO host. The emission arising from the $^5D_0 \rightarrow ^7F_1$ transition has been associated with the magnetic dipole, while the emission arising from the $^5D_0 \rightarrow ^7F_2$ transition is ascribed to the electric dipole [55]. Since the emission arising from the $^5D_0 \rightarrow ^7F_2$ transition was the stronger emission, this indicates that the Eu ions occupied sites without inversion symmetry [56], which is consistent with the Zn^{2+} lattice sites. But the symmetry in the ZnO unit cell is deteriorated by the simultaneous presence of Eu^{2+} and Eu^{3+} , as discussed in XRD section, and can explain the relatively broadening of the PL emission peaks. As the emission ascribed to the $^5D_0 \rightarrow ^7F_0$ transition is a sharp line at around 579 nm, it may not be sensitive to the Eu ion surrounding symmetry. The emission of deep-level defects was reduced for the non-annealed doped micropods with an increase in the Eu concentration. Thus, the peaks corresponding to the 4f-4f transitions of Eu^{3+} are more distinct. This change shows a competition between the defect emissions and that of Eu ions, where a higher number of excited charge carriers are trapped by the energy levels of the Eu^{3+} ions rather than by the defects. However, the reverse occurred when the sample was annealed at 700C. In fact, the emission peaks of Eu disappear in the PL spectrum of doped ZnO micropods and annealed at 700C (figure 12 (b)). The defect concentration was so high that the emission overlapped with that of Eu^{3+} . The 4f-4f characteristic emission was only observed for the sample with 1.92 % Eu. It is therefore the optimal sample that has a higher intensity 4f-4f and exceeds the ZnO defect emission, although it contains a high defect concentration, as shown by the SEM analysis. It is a known rare earth (RE^{3+}) emitted in the visible-IR spectral region, resulting in stable and multiple

sharp bands at a single excitation. However for our sample, no intense sharp peaks have been seen in all PL spectra excited at 325 nm except for those as grown where the emission of the $^5D_0 \rightarrow ^7F_2$ transition protrude from the deep level emission. These results clearly demonstrate that the 325 nm light source excites the ZnO micropods with an inefficient (weak) energy transfer to Eu^{3+} . When the samples were excited at 325 nm, the electrons in the valence band absorbed energy and moved to the conduction band in the ZnO host. Thereafter, some of them return to the valence band, and thus we obtain the band-edge emission. In parallel, the other electrons return to the valence band after they are captured and trapped by various defect and dopant levels. The de-excitation via Eu^{3+} ion energy levels occurred as the 4f-4f transition peaks appeared in the PL spectrum excited at 405 nm, but they were not dominant for the annealed samples. Therefore, the defect concentration was higher for the annealed samples, so its emissions cover the 4f-4f emission of rare earth ions. No evidence of an efficient energy transfer between ZnO and the different energy levels of the rare-earth ions introduced into the band gap of ZnO can be deduced from our PL measurement, contrary to what has been reported in the literature [9,57]. Figure 13 shows a schematic band diagram of the emissions in the Eu-doped ZnO micropods deduced from the PL data excited at 325 and 405 nm. Upon excitation at 325 nm, the recombination of carriers from the CB to the VB gives the UV emission. The relaxed carriers are trapped at the level of the ZnO defects and the 5D_0 level, given the broad visible emission and resonant luminescence characteristics of Eu^{3+} , respectively. Energy transfer from the carriers trapped at the ZnO defect levels to the dopant levels occurs, as reported by Jouad et al. [58]. However, the emission of deep-level defects overlaps that of Eu^{3+} ions. In contrast, when the sample was excited at 405 nm, The $^5D_0 \rightarrow ^7F_i$ ($i=0-5$) transitions dominated that of the ZnO defects and distinct emission peaks were observed in the PL spectra. The deformation of the visible emission band as a function of heat treatment and/or Eu concentration can be explained by the charge imbalance of Eu^{3+} inside ZnO, which causes local negative charge defects such as interstitial O and Zn/O vacancies. Consequently, local positive charge defects could inevitably appear inducing lattice defects, thus generating new and/or perturbing energy levels in the band gap of ZnO. Taking the intensity data of the PL emission spectrum within respectively 380 nm-750 nm and 500 nm-750 nm, chromaticity coordinates (x,y) for our samples excited at 325nm and at 405 nm has been calculated using CIE color soft-ware. The corresponding (x, y) color coordinates are given in Table 8, and their positions in the CIE 1931 xy chromaticity coordinate diagram are presented in Figure 14 and 15. The calculated CIE color coordinates at excitation 325 were

found to be in the ranges of $0.392 \leq x \leq 0.536$ and $0.449 \leq y \leq 0.315$. Based on the National Television Standard Committee (NTSC) system, the ideal red-emitting CIE (Commission International de l'Eclairage) coordinates are $x = 0.67$ and $y = 0.33$ [10]. Therefore, our obtained coordinates are relatively weaker [57], but closer to those reported by Kumar et al. [11] and Hasabeldaim et al. [8]. For the as-grown sample, the color coordinates were found to be in the orange region, and the Eu concentration did not have a significant effect. For the undoped sample annealed at 300C, the color coordinates are in the purplish-pink region, but as the Eu concentration increases, (x,y) becomes in yellowish-pink region. The CIE chromaticity diagram shows that the color of the annealed sample at 500C falls in a large range from orange-yellow emission to reddish-orange emission depending on the Eu concentration. Among the samples studied, the richness red emission was obtained for ZnO micropods doped with a higher Eu concentration and annealed at 500C. The CIE chromaticity diagram of undoped and doped ZnO micropods with the same Eu concentration ($X_{Eu} \cong 1.1\%$) for different annealing temperatures is shown in Figure 16. The increase in T_a appears to be disastrous for obtaining the desired red color; indeed, the color emission for the annealed samples moved away from the red region in the CIE chromaticity diagram. Because the spectral region (500 nm-750 nm) was not sufficient to measure the CIE coordinates and the samples were excited at 405 nm, the CIE data obtained are approximations, but is a good illustration of the competition between the emission of ZnO defects and that of Eu ions. For the as-grown sample, the color coordinates (figure 15 (a)) were shifted deeper in the orange region as the Eu concentration increased. This is due to the emission of rare earth ions, which outweighs the defect emission of the ZnO host. However, for the samples annealed at 700C, the (x,y) coordinate (figure 15 (b)) shifts from the yellow to yellow green region as X_{Eu} increases up to 1.72%, which proves that the defect emission is dominant. This tendency was reversed at higher concentrations, and the emission of the sample was orange yellow. Similar results were reported by Hasabeldaim et al. [55]. Thus, the incorporation of a greater quantity of Eu without any heat treatment should lead to the emission of the desired red color in our samples. Another parameter, the correlated color temperature (CCT), which indicates the color appearance of a light source, is very important and is required for suitable lighting applications in different areas. It can be calculated based on the CIE color coordinate (x,y) using the McCamy empirical [57]:

$$CCT = -437n^3 + 3601n^2 - 6861n + 5541.31, \quad (9)$$

Where $n = (x - x_c)/(y - y_c)$ and $x_c=0.3320$, $y_c=0.1858$ are the epicenter chromaticity coordinate. CCT values below 5000 K (i.e., warm CCTs) are suitable for public and living areas; however, CCT values higher than 5000 K (cool CCTs) are used to enhance concentration, for example in schools, working areas, and shopping centers. The calculated CCT values for our samples are given in Table 8, and their variation as a function of Eu concentration incorporated in ZnO micropods for the different annealing temperatures are shown in Figure 17. All values, except un-doped and 1.20% Eu-doped ZnO annealed at 700C, are smaller than 5000 K, indicating that these samples can be used to perform warm LEDs suitable for living and residential areas. The CCT values of the doped samples show a weak decrease with increasing concentration of Eu incorporated, whereas for annealed samples ($T_a \leq 500C$), they decrease practically linearly with the same slope. The CCT values of the samples without heat treatment were slightly larger than those reported by Singh et al. [9] (and references therein) for Eu-ZnO nanopowders prepared by precipitation and calcined at different temperatures.

3.7 Current-voltage measurements

To determine the electrical parameters of the Eu-doped ZnO micropods on the p-Si substrate heterojunction, I-V measurements were conducted in the dark at room temperature and are presented in Figure 18. All I-V characteristics exhibited successful p-n heterojunction formation. The rectification ratios (I_F/I_R) calculated at $\pm 4V$ for the various heterojunctions are listed in Table 9. It should be noted that the current intensity does not vary monotonically with increasing Eu concentration. It is worth mentioning that the I-V plots are the average results of all micropods under the area considered. Therefore, the non-uniformity of the substrate coverage by the micropods, as seen in the SEM images, is the cause of the current intensity variation with X_{Eu} . A non-saturating behavior of the reverse current is observed for some samples, which is caused by barrier inhomogeneities at the ZnO micropods/p-Si interface. When the reverse bias is increased, a current can flow through the lower barrier height regions, leading to a greater current flow [59]. This phenomenon is responsible for the weak values of the rectification ratio and their variation from one sample to another. The current of the diode depends on the carrier concentration variation, majority carrier recombination in the pn junction, and minority diffusion current at the interface. Native ZnO defects play an important role in the electrical properties of ZnO. In particular, oxygen vacancies (V_O) are recognized as defects that contribute to the concentration of free carriers, conductivity, and electronic mobility of n-type ZnO. For un-doped ZnO micropods, a better

rectification ratio is ≈ 6 for micropods annealed at 500C which are smaller than our results ($I_F/I_R=54$ at 2V) [17] obtained for well aligned and perpendicular nanorods on p-Si substrate and that reported by Gayen et al. [59] ($I_F/I_R=40$ at $\pm 4V$). The low value of the rectification ratio obtained can be due to the low concentration of oxygen vacancies, as seen by XPS and the high dislocation density. Although the ZnO micropod heterojunction presented a higher ratio area of the oxygen vacancy concentration, the rectification ratio was small. This is probably due to the micrometer size of the pods and their non-uniformity coverage of the substrate. In fact, the area of the micropods that is in contact with the substrate below and the metal contact combined with the tilt and the difference in size of micropods reduce the leakage current. In contrast, a rectification ratio of 15 at ± 5 V was obtained by Lu et al. [60] for heterojunctions without a buffer layer, and it reached 429 at 5 V for a heterojunction with a 5 nm thick buffer Al_2O_3 layer. Using a 60 nm thin layer of ZnO deposited by spin coating, Gayen et al. [59] reported a 40 rectification ratio at $\pm 4V$. In fact, the presence of a buffer layer minimizes the lattice mismatch between the ZnO layer and Si substrate. For doped micropods, the rectification ratio is small and reach 21.6 for higher Eu concentration incorporated and higher annealing temperature (700C). This sample presents a lower ratio area of oxygen vacancy concentration and relatively low-density dislocation. Therefore, the incorporation of Eu reduces the oxygen deficiencies (Table 2) and may lead to a decrease in the concentration of free carriers, resulting in an increase in the depletion region width at the interface between the np-junctions, and consequently, a low rectification ratio. In addition the presence of dislocations, as confirmed by X-ray diffraction, whose density varies as a function of the concentration of Eu and the variation of the contact surface between micropods and the substrate from one sample to another explains the divergences obtained on the electrical parameters of the different heterojunctions. Therefore, the non-annealing heterojunction and the deposition of a ZnO buffer layer on the substrate before the growth of the micropods should increase the rectification ratio. In order to determine the electrical parameters of our heterojunction and assuming that the current is due to a thermionic emission (TE) [60], we consider the relation between the applied forward bias and the current given by [61]:

$$I = I_s \left[\exp\left(\frac{q(V - IR_s)}{nKT}\right) - 1 \right], \quad (10)$$

where I_s is the saturation current, q is the electronic charge, V is the applied voltage, n is the ideality factor, K is the Boltzmann constant ($1.38 \cdot 10^{-23}$ J/K), T is the absolute temperature, and IR_s is the voltage drop across a series of resistances R_s . In Fact, the I-V behavior of the

diode is affected by parasitic resistances such as series resistance (R_s), so the voltage drop across the heterojunction is acquired by subtracting from the applied voltage across the series resistance [61]. The saturation current I_s is defined by [62]:

$$I_s = AA^* T^2 \exp\left(-\frac{q\phi_b}{KT}\right), \quad (11)$$

where A is the surface of the diode, A^* is the effective Richardson's constant of ZnO ($32 \text{ A cm}^{-2} \text{ K}^{-2}$) [62], ϕ_b is the barrier height, which can be calculated from the following relation:

$$\phi_b = \frac{KT}{q} \ln\left(\frac{AA^*T^2}{I_s}\right), \quad (12)$$

When the polarization exceeded a certain threshold ($V \geq 3kT/q$), the I-V characteristic changes and presents a certain linearity (ohmic regime). In this area, the conduction is limited by the volume of the semiconductor. We obtained the best-fit straight line for the linear portion of the I-V characteristic at high voltage, where its inverse slope is the series resistance (R_s) and the intersection value with the voltage axis is the turn-on (threshold) voltage (V_F). The reverse saturation current (I_s) can be derived from the intercept of the straight line of $\ln(I)$ at $V=0$; however, the ideality factor n can be determined from the slope of the linear straight line of the direct polarization of the curve $\ln(I) - V$. The equation that yields n is expressed as follows:

$$n = \frac{q}{KT} \frac{d(V - IR_s)}{d\ln(I)}, \quad (13)$$

The corresponding values of the turn-on voltage (V_F), reverse saturation current (I_s), ideality factor (n), barrier height (ϕ_b), and series resistance (R_s) were extracted for all our heterojunctions and are summarized in Table 9. This extraction of electrical parameters is referred to as the standard I-V method. Cheung–Cheung has also been used [63]. The parameters are determined by the following functions derived from I–V characteristics, as detailed in [63]:

$$\frac{dV}{d\ln(I)} = \frac{nKT}{q} + IR_s, \quad (14)$$

$$H(I) = V - \left(\frac{nKT}{q}\right) \ln\left(\frac{I}{AA^*T^2}\right) = n\phi_b + IR_s, \quad (15)$$

R_s and n can be determined from the slope of the $dV/d(\ln I)$ versus I plot and y axis intercept, respectively. Using the determined n , $H(I)$ versus I plot shows a straight line, the slope of this plot gives the series resistance R_s , and height barrier ϕ_b can be determined using the equation ($H(I)$) from the y-axis intercept. The results obtained using Cheung–Cheung method are listed

in Table 9. Figure 19 shows $dV/d(\ln I)$ and $H(I)$ versus I plots for the undoped sample and $X_{Eu}=2.54\%$ doped ZnO annealed at 700C. For our samples, the turn-on voltage are comprised between 1.80 V and 3.36V except that of the un-doped ZnO micropods annealed at 700C where $V_F=0.69$ V. Our values are lower than those reported by Hasabeldaim et al. [32] about 10 V for Eu (3 mol%) doped ZnO thin films were deposited by pulsed laser deposition at different oxygen partial pressures and then obtained by Bedia et al. [64] 11.5V for the n-ZnO/p-Si heterojunction prepared by spray pyrolysis technique. A turn-on voltage of 0.6 V was obtained by Faraz et al. [61] for ZnO nanorods grown on a p-silicon substrate by an aqueous chemical growth method, similar to our value for ZnO micropods annealed at 700C. Based on our results, the ideality factor of the ZnO/Si heterojunction was calculated to be 1.51, 1.36, 3.33 and 1.27 for non and annealed at 300C, 500C and 700C respectively, greater than the ideal value ($n = 1$). The high value of the ideality factor is attributed to the series resistance and the presence of interface states [47]. The barrier height for non-doped heterojunction vary slightly from 0.81 eV to 0.87 eV with the anneal temperature. These values are greater than those reported by Faraz et al. ([61] and references therein) and our result (0.62 eV) for well-aligned ZnO nanorods on Si [17], probably due to the difference in diameter. No significant change in the ideality factor and barrier height determined by the standard method was observed for Eu-doped heterojunctions compared to un-doped heterojunctions. Compared to the electrical parameters obtained by Turgut et al. [47] for Al/n-ZnO:Eu/p-Si heterojunction diodes, where Eu-doped ZnO thin films are coated on p-Si substrates via a sol-gel route by using a spin coater, their barrier height are close to our obtained values and a similar order of ideality factor can be seen except for higher Eu concentration ($x=2.54\%$) incorporated in ZnO micropods.

For an ideal diode, (n) should be equal to unity, which indicates that there is only pure thermionic emission. Therefore, additive mechanisms contribute to carrier transport across heterojunctions. The high n values in the dark condition can be caused by the presence of interface states/traps, barrier inhomogeneities at the metal/semiconductor interface, series resistance, formation of an oxide interlayer, and generation-recombination events in the space charge zone [63]. The series resistance values of our heterostructures extracted by the two methods are very large, a few tens of $k\Omega$, compared to those reported in the literature for thin films [63] and nanorods [61] because of the irregular contact at the micropod/substrate interface. The series resistance determined by the Cheung-Cheung method is higher than that determined by the standard method, which explains the difference in the electrical parameter values obtained by the two methods for our heterojunction diodes. The ϕ_b values derived from

the two methods are similar, indicating that these procedures are trustworthy and that the differences in R_s and n may be due to the extraction of data from different regions of the forward bias (I-V) plot [65]. The electronic properties of semiconductors are greatly influenced by the presence of disorder, impurities, or defects. These are responsible for creating electronic states that do not exist in perfectly crystalline semiconductors. These states can be generated in the volume of the material, on its surface, or at the interfaces present during the preparation of devices that affect the I-V characteristic differently from one voltage range to another.

4. Conclusions

Undoped and Eu-doped micropod-like ZnO on p-Si were synthesized by the CBD technique at a bath temperature of 87°C without phase segregation, as confirmed by X-ray diffraction. The incorporation of Eu increased with the annealing temperature and reached 2.54. XPS spectra confirmed the simultaneous presence of Eu^{2+} and Eu^{3+} in the doped micropods. XRD and SEM results showed that the micropods had a hexagonal wurtzite structure with smooth sidewalls. The interstitial sites occupied by Eu^{3+} ions distorted the four tetrahedral bonds. However, Eu^{2+} ions, which substituted Zn^{2+} ions, increased the c lattice parameter, while maintaining the c/a ratio. The intensity of the UV emission excited at 325 nm for the samples annealed at 300°C was higher than that of the visible emission, which can be useful for UV random lasing applications. The visible emission was significantly enhanced for the other samples, indicating a higher density of induced defects, partly because of the disorder caused by Eu incorporation. PL measurements at an excitation wavelength of 325 nm did not reveal the resonant luminescence characteristics of the Eu^{3+} ions. Thus, an efficient energy transfer between ZnO and rare-earth ions could not be highlighted, although the insertion of Eu ions into ZnO was demonstrated. Upon direct excitation of Eu^{3+} ions (with $\lambda_{\text{exc}}=405$ nm), the 4f-4f transition emission dominates the ZnO defect emission as the Eu concentration increases for doped ZnO micropods without heat treatment. A possible transfer energy between the ZnO defect level and the Eu dopant was demonstrated. Interestingly, sample color emission may be controlled by the Eu concentration and annealing temperature. Based on the CIE results, the prepared Eu-doped ZnO micropods (orange-yellow and reddish-orange) may be useful for different luminescent applications, including warm light, especially in living and residential areas. The I-V measurements revealed a p-n heterojunction formation for all the samples. The extracted electrical parameters show a slight variation in barrier height ϕ_b . However, a

low rectification ratio and a very high series resistance compared with those reported in previous studies were found.

ACKNOWLEDGMENTS

The authors take this opportunity to thank the Department of Physics, College of Science at Zulfi, Majmaah University, specifically Dr. Ibrahim Shaarany, for helpful technical assistance with equipment facilities.

Conflict of interest The authors declare that they have no conflict of interest.

Credit author statement

Nouf Ahmed Althumairi: Conceptualization, Validation, Investigation, Writing - Original Draft. **Irshad Baig:** Investigation. **Tarek Said Kayed:** Investigation. **Abdelkarim Mekki:** Investigation, Validation, Writing - Review & Editing . **Alain Lusson:** Investigation, Validation. **Vincent Sallet:** Investigation. **Abdul Majid:** Investigation. **Afif Fouzri:** Conceptualization, Validation, Investigation, Writing - Original Draft, Writing - Review & Editing, Visualization, Supervision.

References

- 1- Ü. Özgür, Ya. I. Alivov, C. Liu, A. Teke, M. A. Reshchikov, S. Doğan, V. Avrutin, S.-J. Cho, and H. Morkoç , A comprehensive review of ZnO materials and devices, *Journal of Applied Physics* 98 (2005) 041301.
- 2- M. Willander, O. Nur, Q. Zhao, L. Yang, M. Lorenz, B. Cao et al., Zinc oxide nanorod based photonic devices: Recent progress in growth, *Nanotechnology* 20 (2009) 332001.
- 3- M. Law, L. Greene, J. Johnson, R. Saykally, P. Yang, Nanowire dye-sensitized solar cells, *Nat. Mater.* 4 (2005) 455-464.
- 4- M. Samadi, M. Zirak, A. Naseri, E. Khorashadizade, A.Z. Moshfegh, Recent progress on doped ZnO nanostructures for visible-light photocatalysis, *Thin Solid Films* 605 (2015) 2–19.
- 5- P. Camarda, F. Messina, L. Vaccaro, S. Agnello, G. Buscarino, R. Schneider, R. Popescu, D. Gerthsen, R. Lorenzi, F.M. Gelardi, M. Cannas, Luminescence mechanisms of defective ZnO nanoparticles, *Phys. Chem. Chem. Phys.* 18 (2016) 16237-16244.
- 6- K. Deva Arun Kumar, S. Valanarasu, A. Kathalingam, V. Ganesh, Mohd Shkir, S. AlFaify, Effect of solvents on sol-gel spin-coated nanostructured Al-doped ZnO thin films: a film for key optoelectronic applications, *Appl. Phys. A Mater.* 123 (2017) 1-11.
- 7- H. Shahroosvand, M. Ghorbani-asl, Solution-based synthetic strategies for Eu doped ZnO nanoparticle with enhanced red photoluminescence, *J. Lumin.* 144 (2013) 223–229
- 8- E. Hasabeldaim, O. Ntwaeaborwa, R. Kroon, E. Coetsee, H. Swart, Photoluminescence and cathodoluminescence of spin coated ZnO films with different concentration of Eu^{3+} ions, *Vacuum* 169 (2019) 108889.
- 9- A. Singh, P. Arya, D. Choudhary, S. Kumar, A. K. Srivastava, I. B. Singh, Cost-effective ZnO– Eu^{3+} films with efficient energy transfer between host and dopant, *SN Appl. Sci.* 2 (2020) 870-878.
- 10- K. Park, D. Hakeem, J. Pi, G. Jung, Emission enhancement of Eu^{3+} -doped ZnO by adding charge compensators, *J. Alloy. Compd.* 772 (2019) 1040-1051.
- 11- V. Kumar, V. Kumar, S. Som, M. Duvenhage, O. Ntwaeaborwa, H. Swart, Effect of Eu doping on the photoluminescence properties of ZnO nanophosphors for red emission applications, *Appl. Surf. Sci.* 308 (2014) 419-430.
- 12- L. Yang, Zh Jiang, J. Dong, A. Pan, X. Zhuang, The study the crystal defect-involved energy transfer process of Eu^{3+} doped ZnO lattice, *Mater. Lett.* 129 (2014) 65–67.

- 13- L. Luo, F.Y. Huang, G.J. Guo, P.A. Tanner, J. Chen, Y.T. Tao, J. Zhuo, L.Y. Yuan, S.Y. Chen, Y.L. Chueh, H.H. Fan, K.F. Li, K.W. Cheah, Efficient doping and energy transfer from ZnO to Eu³⁺ ions in Eu³⁺-doped ZnO nanocrystals, *J. Nanosci. Nanotechnol.* 12 (2012) 2417–2423.
- 14- H.J. Lozykowski, Kinetics of luminescence of isoelectronic rare-earth ions in III-V semiconductors, *Phys. Rev. B* 48 (1993) 17758–17769.
- 15- A. Nouri, A. Beniaiche, B.M. Soucase, H. Guessas, A. Azizi, Photoluminescence study of Eu³⁺ doped ZnO nanocolumns prepared by electrodeposition method, *Optik* 139 (2017) 104-110.
- 16- André Felipe Vale da Fonseca, Renato Luiz Siqueira, Richard Landers, Jefferson Luis Ferrari, Naiara L. Marana, Júlio R. Sambrano, Felipe de Almeida La Porta, Marco Antônio Schiavon, A theoretical and experimental investigation of Eu-doped ZnO nanorods and its application on dye sensitized solar cells, *Journal of Alloys and Compounds* 739 (2018) 939-947.
- 17- W. Chebil, A. Gokarna, A. Fouzri, N. Hamdaoui, K. Nomenyo and G Lerondel, Study of the growth time effect on the structural, morphological and electrical characteristics of ZnO/p-Si heterojunction diodes grown by Sol-gel assisted chemical bath deposition method, *Journal of Alloys and Compounds* 771 (2019) 448-455.
- 18- Y. Ching-Jung, W. Shun-Min, L. Shih-Wei, C. Yung-Huang, C. Chih, S. Jia-Min, Low-temperature growth of ZnO nanorods in anodic aluminum oxide on Si substrate by atomic layer deposition, *Appl. Phys. Lett.* 90 (2007) 033104.
- 19- A. Gokarna, R. Aad, J. Zhou, K. Nomenyo, A. Lusson, P. Miska, G. Lerondel, On the origin of the enhancement of defect related visible emission in annealed ZnO micropods, *J. Appl. Phys.* 126 (2019) 145104.
- 20- R. Galeazzi, I.J. Gonzalez-Panzo, T. Diaz-Becerril, C. Morales, E. Rosendo, R. Silva, R. Romano-Trujillo, A. Coyopol, F.G. Nieto-Caballeroc, L. Trevino- Yarcea, Physicochemical conditions for ZnO films deposited by microwave chemical bath deposition, *RSC Adv.* 8 (2018) 8662-8670.
- 21- G. Greczynski, L. Hultman, Reliable determination of chemical state in x-ray photoelectron spectroscopy based on sample-work-function referencing to adventitious carbon: Resolving the myth of apparent constant binding energy of the C 1s peak, *Appl. Surf. Sci.* 451 (2018) 99-103.

- 22- P.-C. Lee, Y.-C. Ou, R.-C Wang, C.-P. Liu, Enhanced output performance of ZnO thin film triboelectric nanogenerators by leveraging surface limited ga doping and insulting bulk, *Nano Energy* 89 (2021) 106394.
- 23- M. H. N. Assadi, Y. Zhang, R. K. Zheng, S. P. Ringer, S. Li, Structural and Electronic Properties of Eu-and Pd-doped ZnO, *Nanoscale Research Letters* 6 (2011) 357-364.
- 24- P. Che, J. Meng, L. Guo, Oriented growth and luminescence of ZnO:Eu films prepared by sol-gel process, *Journal of Luminescence* 122-123 (2007) 168-171.
- 25- Y.-P. Du, Y.-W. Zhang, L.-D. Sun and C.-H. Yan, Efficient Energy Transfer in Monodisperse Eu-Doped ZnO Nanocrystals Synthesized from Metal Acetylacetonates in High-Boiling Solvents, *The Journal of Physical Chemistry C* 112 (2008) 12234-12241.
- 26- B. Cao, W. Cai, From ZnO Nanorods to Nanoplates: Chemical Bath Deposition Growth and Surface-Related Emissions, *J. Phys. Chem. C* 112 (2008) 680-685.
- 27- R. Majitha, J. Speich, K. E. Meissner, Mechanism of Generation of ZnO Microstructures by Microwave-Assisted Hydrothermal Approach, *Materials* 6 (2013) 2497-2507.
- 28- J. F. Moulder, *Handbook of X-Ray Photoelectron Spectroscopy: a Reference Book of Standard Spectra for Identification and Interpretation of XPS Data*, Physical Electronics Division, Perkin-Elmer Corporation, Chicago, 1995.
- 29- S. Dhara, K. Imakita, M. Mizuhata, M. Fujii, Europium doping induced symmetry deviation and its impact on the second harmonic generation of doped ZnO nanowires, *Nanotechnology* 25 (2014) 225202.
- 30- I. Ahmad, M. S. Akhtar, E. Ahmed, M. Ahmad, V. Keller, et al., Rare earth co-doped ZnO photocatalysts: Solution combustion synthesis and environmental applications, *Separation and Purification Technology*, 237 (2020) 116328
- 31- U. Alam, A. Khan, W. Raza, A. Khan, D. Bahnemann, M. Muneer, Highly efficient Y and V co-doped ZnO photocatalyst with enhanced dye sensitized visible light photocatalytic activity, *Catalysis Today* 284 (2017) 169-178.
- 32- E. H. H. Hasabeldaim, O. M. Ntwaeaborwa, R. E. Kroon, E. Coetsee, H. C. Swart, Luminescence properties of Eu doped ZnO PLD thin films: The effect of oxygen partial pressure, *Superlattices and Microstructures* 139 (2020) 106432.
- 33- K. Kotsis, V. Staemmler, Ab initio calculations of the O1s XPS spectra of ZnO and Zn oxo compounds” *Phys. Chem. Chem. Phys.* 8 (2006) 1490-1498.
- 34- L. Jiang, J. Li, K. Huang, S. Li, Q. Wang, Z. Sun, T. Mei, J. Wang, L. Zhang, N. Wang, X. Wang, Low-Temperature and Solution-Processable Zinc Oxide Transistors for Transparent Electronics, *ACS Omega* 2 (2017) 8990-8996.

- 35- V. Kumar, O. M. Ntwaeaborwa, T. Soga, V. Dutta, H. C. Swart, Rare Earth Doped Zinc Oxide Nanophosphor Powder: A Future Material for Solid State Lighting and Solar Cells, *ACS Photonics* 4(11) (2017) 2613-2637.
- 36- V. Kumar, S. K. Swami, A. Kumar, O.M. Ntwaeaborwa, V. Dutta, H.C. Swart, Eu^{3+} doped down shifting TiO_2 layer for efficient dye-sensitized solar cells, 484 (2016) 24-32.
- 37- J. Petersen, C. Brimont, M. Gallart, G. Schmerber, P. Gilliot, C. Ulhaq-Bouillet, J-L Rehspringer, S. Colis, C. Becker, A. Slaoui, A Dinia, Correlation of structural properties with energy transfer of Eu-doped ZnO thin films prepared by sol-gel process and magnetron reactive sputtering, *journal of applied physics* 107 (2010) 123522.
- 38- S. M. Ahmed, P. Szymanski, M. A. El-Sayed, Y. Badr, L. M. El-Nadi, The photoluminescence properties of undoped & Eu-doped ZnO thin films grown by RF sputtering on sapphire and silicon substrates, *Appl. Surf. Sci.* 359 (2015) 356-363.
- 39- F. H. Cameron, E. S. Raymond, Tutorial on Powder X-ray Diffraction for Characterizing Nanoscale Materials. *ACS Nano* 13 (2019) 7359–7365.
- 40- W. Chebil, A. Fouzri, N. Sakly, A. Lusson and V. Sallet, Comparison of ZnO thin films on different substrates obtained by sol-gel process and deposited by spin-coating technique, *Indian journal of pure and applied physics* 53 (8), 521-529, (2015).
- 41- A. Fouzri, N. A. Althumairi, V. Sallet, A. Lusson, Characterization of sol gel $\text{Zn}_{1-x}\text{Ca}_x\text{O}$ thin layers deposited on p-Si substrate by spin-coating method, *Optical Materials* 110 (2020) 110519
- 42- E. Sakellis, A. Markopoulos, C. Tzouvelekis, M. Chatzigeorgiou, A. Travlos, N. Boukos, Low-Cost Electrodeposition of Size-Tunable Single-Crystal ZnO Nanorods, *Fibers* 9 (2021) 38-49.
- 43- H. Morkoç, Ü. Özgür, Zinc Oxide: Fundamentals, Materials and Device Technology; WILEY_VCH Verlag GmbH and KGaA, Weinheim, 2009.
- 44- F. Otieno, M. Airo, R. M. Erasmus, A. Quandt, D. G. Billing, D. Wamwangi, Annealing effect on the structural and optical behavior of $\text{ZnO}:\text{Eu}^{3+}$ thin film grown using RF magnetron sputtering technique and application to dye sensitized solar cells, *Sci Rep*, 10 (2020) 8557.
- 45- C.-M. Lin, H.-T. Liu, S.-Y. Zhong, C.-H. Hsu, Y.-T. Chiu, M.-F. Tai, J.-Y. Juang, Y.-C. Chuang, Y.-F. Liao, Structural Transitions in Nanosized $\text{Zn}_{0.97}\text{Al}_{0.03}\text{O}$ Powders under High Pressure Analyzed by in Situ Angle-Dispersive X-ray Diffraction, *Materials* 9 (2016) 561-568.

- 46- L. Arda, The effects of Tb doped ZnO nanorod: An EPR study, *Journal of Magnetism and Magnetic Materials* 475 (2019) 493–501.
- 47- G. Turgut, S. Duman, E. Sonmez, F.S. Ozcelik, A study of Eu incorporated ZnO thin films: An application of Al/ZnO:Eu/p-Si heterojunction diode, *Materials Science and Engineering B* 206 (2016) 9–16.
- 48- M. Kaur, P. Kaur, G. Kaur, K. Dev, P. Negi, R. Sharma, Structural, morphological and optical properties of Eu-N co-doped zinc oxide nanoparticles synthesized using co-precipitation technique, *Vacuum* 155 (2018) 689–695.
- 49- G. Murugadoss, R. Jayavel, M. Rajesh Kumar, Structural and optical properties of highly crystalline Ce, Eu and co-doped ZnO nanorods, superlattices and microstructures 82 (2015) 538-550.
- 50- M. Khuili, N. Fazouan, H. Abou El Makarim, E.H. Atmani, D.P. Rai, M. Houmad, First-principles calculations of rare earth (RE=Tm, Yb, Ce) doped ZnO: Structural, optoelectronic, magnetic, and electrical properties, *Vacuum*, 181 (2020) 109603.
- 51- H. V. S. Pessoni, L. J. QMaia, A. Franco Jr, Eu-doped ZnO nanoparticles prepared by the combustion reaction method: Structural, photoluminescence and dielectric characterization, *Materials Science in Semiconductor Processing* 30 (2015) 135–141.
- 52- A. Galdámez-Martinez, G. Santana, F. Güell, PR. Martínez-Alanis, A. Dutt, Photoluminescence of ZnO Nanowires: A Review. *Nanomaterials (Basel)*. 10 (2020) 857.
- 53- X. Guo, C. P. Tripp, C. Chen, Y. Wang, S. Yin, W. Qin, Temperature dependence of the photoluminescence from ZnO microrods prepared by a float zone method, *CrystEngComm* 18 (2016) 3130-3135.
- 54- A. Lakshmanan, V. Sivakumar, R. Satheesh Kumar, R. Bhaskar, M. T. Jose, N. Lakshminarayan, Synthesis and photoluminescence of Y,Eu co-doped ZnO red phosphor, *Materials Research Bulletin* 47 (2012) 419–424.
- 55- E. Hasabeldaim, O. M. Ntwaeaborwa, R. E. Kroon, H. C. Swart, Structural, optical and photoluminescence properties of Eu doped ZnO thin films prepared by spin coating, *Journal of Molecular Structure* 1192 (2019) 105-114.
- 56- T. T. Van Tran, T. M. Dung Cao, Q. V. Lam, V. H. Le, Emission of Eu^{3+} in SiO_2 -ZnO glass and SiO_2 - SnO_2 glass-ceramic: correlation between structure and optical properties of Eu^{3+} ions, *J. Non-Cryst. Solids* 459 (2017) 57-62.
- 57- R. Singh, A. King, B. B. Nayak, Influence of dopant concentration on powder morphology and photoluminescence characteristics of red-emitting Eu^{3+} -doped ZnO, *Optik*, 247 (2021)16787 .

- 58- M. E. Jouad, E. M. Bouabdalli, S. Touhtouh, M. Addou, N. Ollier, B. Sahraoui, Red luminescence and UV light generation of europium doped zinc oxide thin films for optoelectronic applications, *Eur. Phys. J. Appl. Phys.* 91 (2020) 10501.
- 59- R N Gayen, S R Bhattacharyya, Electrical characteristics and rectification performance of wet chemically synthesized vertically aligned n-ZnO nanowire/p-Si heterojunction, *J. Phys. D: Appl. Phys.* 49 (2016) 115102.
- 60- H-L. Lu, Y-Z. Gu, Y. Zhang, X-Y. Liu, P-F. Wang, Q-Q. Sun, S-J. Ding, D. W. Zhang, Improved photoelectrical properties of n-ZnO/p-Si heterojunction by inserting an optimized thin Al₂O₃ buffer layer, *Opt. Express* 22 (2014) 22184.
- 61- S. M. Faraz, W. Shah, N. Ul Hassan Alvi, O. Nur, Q. Ul Wahab, Electrical Characterization of Si/ZnO Nanorod PN Heterojunction Diode, *Advances in Condensed Matter Physics*, 2020 (2020) 1-9.
- 62- S.O. Tan, İ. Taşcıoğlu, S. Altındal Yerişkin, H. Tecimer, F. Yakuphanoğlu, Illumination Dependent Electrical Data Identification of the CdZnO Interlayered Metal-Semiconductor Structures. *Silicon* 12 (2020) 2885–2891.
- 63- S. K. Akay, S. Sarsıcı, H. K. Kaplan, Determination of electrical parameters of ZnO/Si heterojunction device fabricated by RF magnetron sputtering, *Optical and Quantum Electronics* 50 (2018) 1-11.
- 64- F. Z. Bedia, A. Bedia, B. Benyoucef, S. Hamzaoui, Electrical characterization of n-ZnO/p-Si heterojunction prepared by spray pyrolysis technique, *Physics Procedia* 55 (2014) 61–67.
- 65- N. Balaram, V. R. Reddy, P. S. Reddy, V. Janardhanam, C.-J. Choi, Chemical states and electrical properties of Au/CuO/n-InP heterojunction with a cupric oxide interlayer, 152 (2018) 15-24.

Samples	T _a (C)	X _{Eu} (%)
5%Eu-ZnO	0	1.00
	300	1.04
	500	1.15
	700	1.20
10%Eu-ZnO	0	1.02
	300	1.46
	500	1.57
	700	1.72
15%Eu-ZnO	0	1.28
	300	1.55
	500	1.63
	700	1.92
20%Eu-ZnO	0	1.80
	300	2.20
	500	2.51
	700	2.54

Table 1: Average concentration of europium incorporated in the ZnO annealed at various temperature (T_a) determined by EDX.

Samples	T _a (C)	O1s components	Peak position (eV)	Area ratio (%)
ZnO	0	O ₁	528.64	1.44
		O ₂	530.52	58.99
		O ₃	532.63	39.57
	300	O ₁	530.38	1.33
		O ₂	530.76	56.29
		O ₃	532.19	42.38
	500	O ₁	530.88	8.90
		O ₂	532.21	27.57
		O ₃	532.83	63.53
	700	O ₁	530.19	13.01
		O ₂	531.69	26.68
		O ₃	532.14	60.31
20%Eu-ZnO	0	O ₁	529.22	4.47
		O ₂	530.56	61.53
		O ₃	532.04	34.00
	300	O ₁	530.38	33.27
		O ₂	530.76	36.52
		O ₃	532.19	30.21
	500	O ₁	530.88	72.29
		O ₂	532.21	12.54
		O ₃	532.83	15.17
	700	O ₁	530.19	32.55
		O ₂	531.69	27.19
		O ₃	532.14	40.26

Table 2: Position and area ratio of the three peaks O₁, O₂, O₃ (O–Zn groups, O-deficient groups, O–H groups) at the different annealing temperature for undoped and 20 wt % Eu doped ZnO micropods

T _a (C)	XPS Area			C _{Eu²⁺} (at %)	C _{Eu³⁺} (at %)
	Zn 2p	Eu ²⁺ 3d	Eu ³⁺ 3d		
(As grown)	381213	7732	17024	0.52	1.13
300	596497	20054	26913	0.44	0.45
500	642165	10157	10325	0.41	0.41
700	541825	15473	26478	0.74	1.26

Table 3: Eu²⁺ and Eu³⁺ experimental concentration obtained from XPS measurements for 20 wt % Eu doped ZnO micropods as grown and annealing at 300C, 500C and 700 C. Sensitivity factors (RSF) used are respectively, Zn: 18.92, and Eu: 73.15.

T_a (C)	$X_{Eu}(\%)$	$P_{(100)}$	$P_{(002)}$	$P_{(101)}$
0	0	0.787	0.196	0.017
	1.02	0.884	0.093	0.023
	1.28	0.837	0.128	0.035
	1.80	0.888	0.079	0.033
300	0	0.919	0.068	0.013
	1.04	0.644	0.336	0.020
	1.46	0.876	0.096	0.028
	1.55	0.865	0.082	0.053
	2.20	0.506	0.386	0.108
500	0	0.675	0.241	0.084
	1.15	0.464	0.447	0.089
	1.63	0.845	0.107	0.048
	2.51	0.583	0.297	0.120
700	0	0.830	0.148	0.022
	1.20	0.536	0.418	0.046
	1.72	0.840	0.117	0.043
	1.92	0.851	0.096	0.053
	2.54	0.542	0.363	0.095
ZnO powder	0	0.275	0.225	0.500

Table 4: Preferential orientations parameter $p_{(hkl)}$ as function of Eu concentration in ZnO micropods and for the different annealed temperature. Corresponding parameter of commercial ZnO powder are also given for comparison.

T _a (C)	X _{Eu} (%)	a (Å)	c (Å)	c/a	V (Å ³)	u	b (Å)	b ₁ (Å)
0	0	3.246	5.199	1.602	47.440	0.3799	1.9751	1.9921
	1.02	3.242	5.190	1.601	47.724	0.3801	1.9769	1.9898
	1.28	3.256	5.197	1.601	47.722	0.3800	1.9785	1.9922
	1.80	3.245	5.208	1.605	47.493	0.3794	1.9760	1.9909
300	0	3.240	5.187	1.601	47.156	0.3801	1.9716	1.9885
	1.04	3.246	5.198	1.601	47.431	0.3800	1.9752	1.9922
	1.46	3.250	5.206	1.602	47.621	0.3799	1.9778	1.9945
	1.55	3.249	5.206	1.602	47.592	0.3798	1.9772	1.9939
	2.20	3.247	5.200	1.602	47.479	0.3800	1.9760	1.9928
500	0	3.250	5.206	1.602	47.621	0.3799	1.9778	1.9945
	1.15	3.246	5.198	1.601	47.431	0.3800	1.9752	1.9922
	1.63	3.250	5.200	1.600	47.566	0.3802	1.9770	1.9948
	2.51	3.249	5.204	1.602	47.574	0.3799	1.9770	1.9940
700	0	3.251	5.209	1.602	47.678	0.3798	1.9784	1.9951
	1.20	3.253	5.206	1.600	47.709	0.3801	1.9788	1.9966
	1.72	3.248	5.203	1.602	47.535	0.3799	1.9766	1.9933
	1.92	3.246	5.200	1.602	47.449	0.3799	1.9755	1.9921
	2.54	3.252	5.209	1.602	47.707	0.3799	1.9789	1.9958
ZnO powder	0	3.2502	5.2072	1.6021	47.639	0.3799	1.9780	1.9946
ZnO JCPDS (N° 36-1451)	0	3.2498	5.2066	1.6021	47.849	0.3799	1.9780	1.9944

Table 5: Cell parameters ('a' and 'c'), c/a ratio , unit cell volume, u parameter , bond length b and b₁ as function of Eu concentration and for the different annealed temperature. For comparison structure parameters of commercial powder and those of the JCPDS XRD database, file number 36-1451 are also listed.

T_a (C)	X_{Eu} (%)	$t_{DS}(002)$ (nm)	$\delta_{DS}(200)$ (10^{14} lines/m ²)	$t_{DS}(110)$ (nm)	$\delta_{DS}(110)$ (10^{14} lines/m ²)
0	0	41	5.95	28	12.78
	1.02	42	5.67	31	10.41
	1.28	39	6.57	38	6.93
	1.80	43	5.41	65	2.37
300	0	31	10.41	26	14.79
	1.04	49	4.16	42	5.67
	1.46	48	4.37	35	8.16
	1.55	49	4.16	34	8.65
	2.20	30	11.11	27	13.72
500	0	52	3.73	74	1.83
	1.15	43	5.41	-	-
	1.63	45	4.97	34	8.65
	2.51	38	6.93	35	8.16
700	0	58	2.97	36	7.72
	1.20	45	4.97	34	8.65
	1.72	27	13.72	24	17.36
	1.92	41	5.49	36	7.72
	2.54	44	5.49	35	8.16
ZnO powder	0	30	11.44	33	9.33

Table 6: Debye-Scherrer crystallite sizes and dislocation density for (002) and (110) peaks as function of Eu concentration and for the different annealed temperature. For comparison those of commercial powder are also given.

T _a (C)	X _{Eu} (%)	E _g (eV)	
		Reflectance spectra	PL spectra
0	0	3.20	3.27
	1.02	3.19	3.25
	1.28	3.22	3.27
	1.80	3.25	3.26
300	0	3.19	3.20
	1.04	3.19	3.20
	1.46	3.23	3.19
	1.55	3.24	3.20
	2.20	3.24	3.19
500	0	3.21	3.20
	1.15	3.20	3.18
	1.63	3.22	3.19
	2.51	3.23	3.20
700	0	3.20	3.25
	1.20	3.20	2.25
	1.72	3.20	3.24
	1.92	3.24	3.24
	2.54	3.25	3.23

Table 7: Band gap values of Eu doped ZnO micropods for different Eu concentrations obtained from UV–Vis reflectance and Photoluminescence spectroscopy.

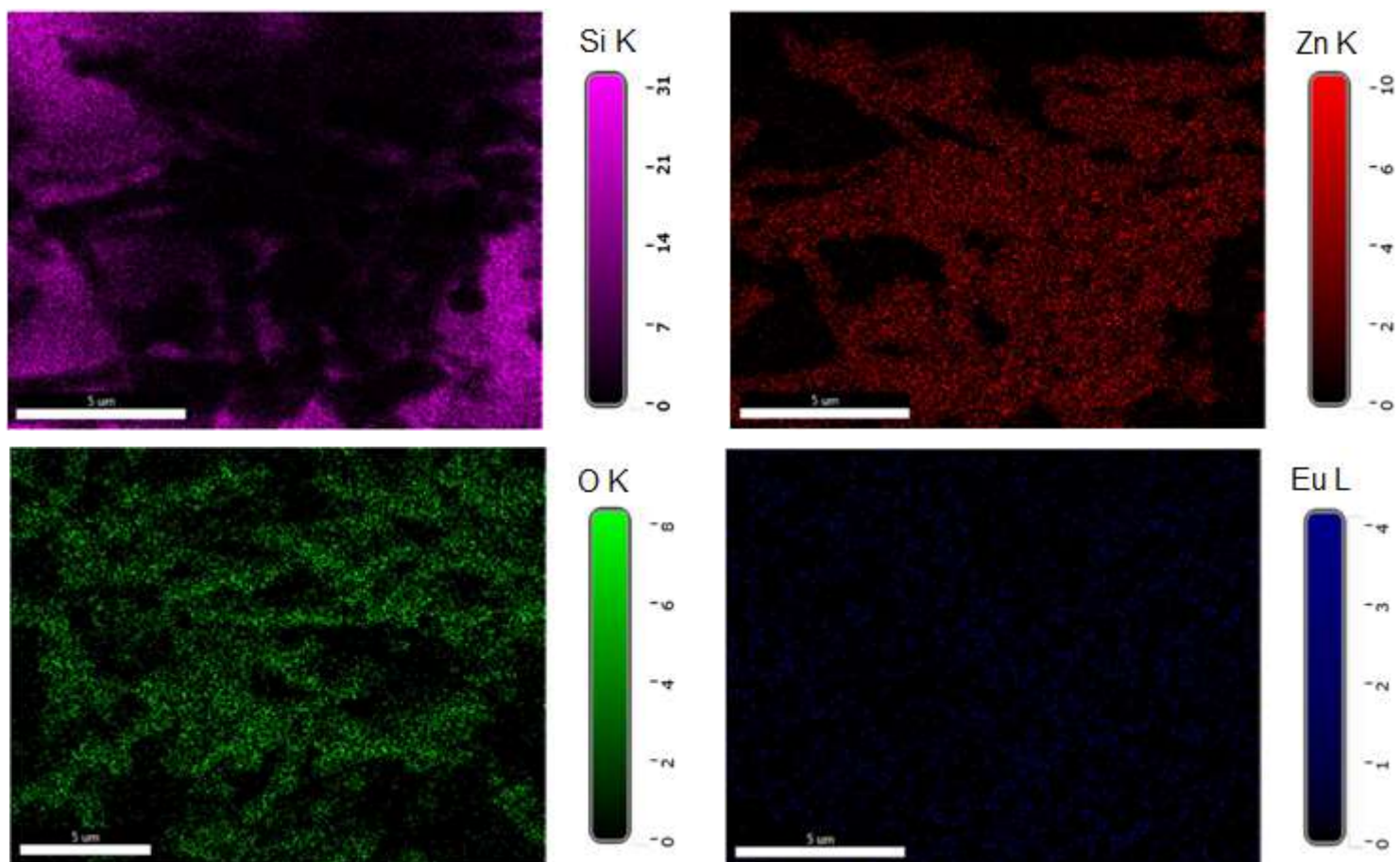
T_a (C)	$X_{Eu}(\%)$	CIE		CCT (K)
		x	y	
		$\lambda_{exc}=325$ nm		
0	0	0.414	0.445	3725
	1.00	0.426	0.455	3573
	1.28	0.435	0.467	3482
	1.80	0.444	0.469	3411
300	0	0.392	0.367	3680
	1.04	0.402	0.315	2818
	1.46	0.432	0.359	2691
	1.55	0.451	0.368	2469
	2.20	0.464	0.368	2293
500	0	0.422	0.449	3598
	1.15	0.440	0.423	3125
	1.63	0.498	0.425	2365
	2.51	0.536	0.376	1786
700	0	0.338	0.451	5378
	1.20	0.320	0.441	5867
	1.72	0.377	0.402	4277
	1.92	0.444	0.405	2907
	2.54	0.445	0.425	2511
T_a (C)	$X_{Eu}(\%)$	$\lambda_{exc}=405$ nm		
0	0	0.481	0.503	3065
	1.00	0.461	0.518	3395
	1.28	0.508	0.480	2638
	1.80	0.512	0.476	2563
700	0	0.451	0.525	3559
	1.20	0.374	0.589	4865
	1.72	0.414	0.552	4181
	1.92	0.519	0.467	2443
	2.54	0.517	0.472	2493

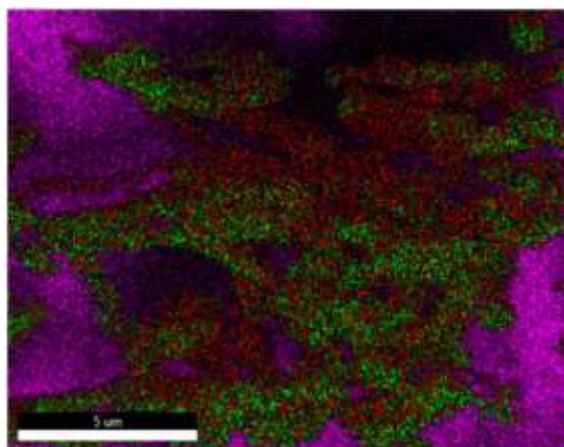
Table 8: Calculated CIE color coordinates for Eu doped ZnO micropods as function of Eu concentration.

T_a (C)	X_{Eu} (%)	I_F/I_R at ± 4 V	Standard I-V method					Cheung - Cheung's method		
			V_F (V)	I_s (10^{-8} A)	n	ϕ_b (eV)	R_s (k Ω)	n	ϕ_b (eV)	R_s (k Ω)
0	0	1.98	3.36	7.15	1.51	0.82	11.7	2.63	0.73	31.8/33.1
	1.02	2.34	1.92	2.40	1.40	0.85	14.9	1.88	0.79	27.5/27.5
	1.28	2.04	1.88	2.34	1.92	0.83	10.6	5.80	0.73	25.6/26.0
	1.80	4.71	1.99	2.38	1.78	0.85	11.1	2.36	0.77	22.5/23.1
300	0	2.48	2.48	9.54	1.36	0.81	15.5	3.14	0.76	34.4/35.4
	1.04	2.19	2.50	2.38	1.53	0.85	18.7	5.54	0.74	37.6/40.2
	1.46	1.98	2.38	5.86	1.54	0.83	30.7	4.50	0.74	45.2/49.7
	1.55	7.60	2.76	7.15	1.68	0.82	10.7	2.58	0.77	25.4/26.2
	2.20	6.04	2.34	2.39	1.28	0.85	17.9	2.70	0.74	37.7/38.3
500	0	6.08	2.27	1.19	3.33	0.87	63.8	3.33	0.77	86.7/89.7
	1.15	6.76	1.80	2.38	1.15	0.85	14.9	1.85	0.80	27.6/27.6
	1.63	7.26	2.83	2.38	1.25	0.86	13.9	5.42	0.77	38.4/41.1
	2.51	4.39	3.22	1.19	1.41	0.86	30.9	5.43	0.77	64.5/68.0
700	0	1.58	0.69	9.54	1.27	0.83	44.4	5.40	0.77	45.9/47.4
	1.20	6.13	2.50	2.38	1.22	0.86	30.7	4.00	0.78	48.8/50.6
	1.75	2.03	2.52	1.19	1.52	0.87	24.4	4.53	0.77	44.9/46.0
	1.92	4.39	3.13	1.19	1.41	0.87	31.5	4.45	0.77	62.5/65.2
	2.54	21.62	3.24	2.38	5.65	0.87	19.0	3.20	0.82	37.9/40.2

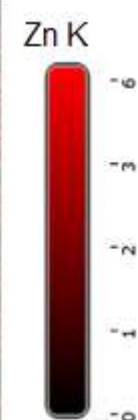
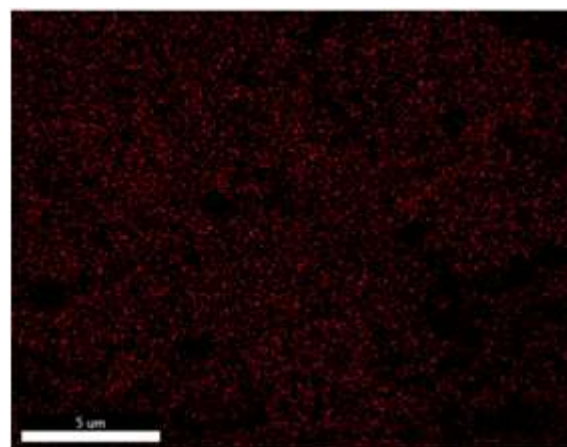
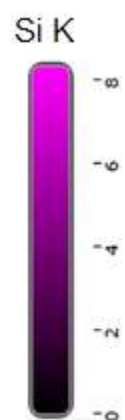
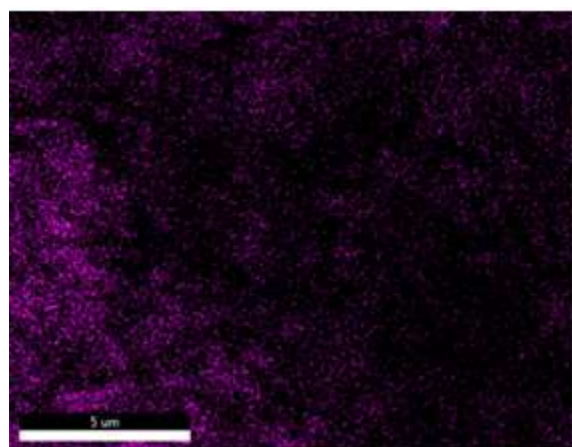
Table 9: The obtained values of rectification ratio (I_F/I_R) calculated at ± 4 V, the turn-on voltage (V_F), the reverse saturation current (I_s), the ideality factor (n), barrier height (ϕ_b) and the series resistance (R_s) for our all samples by two methods.

(a)





(b)



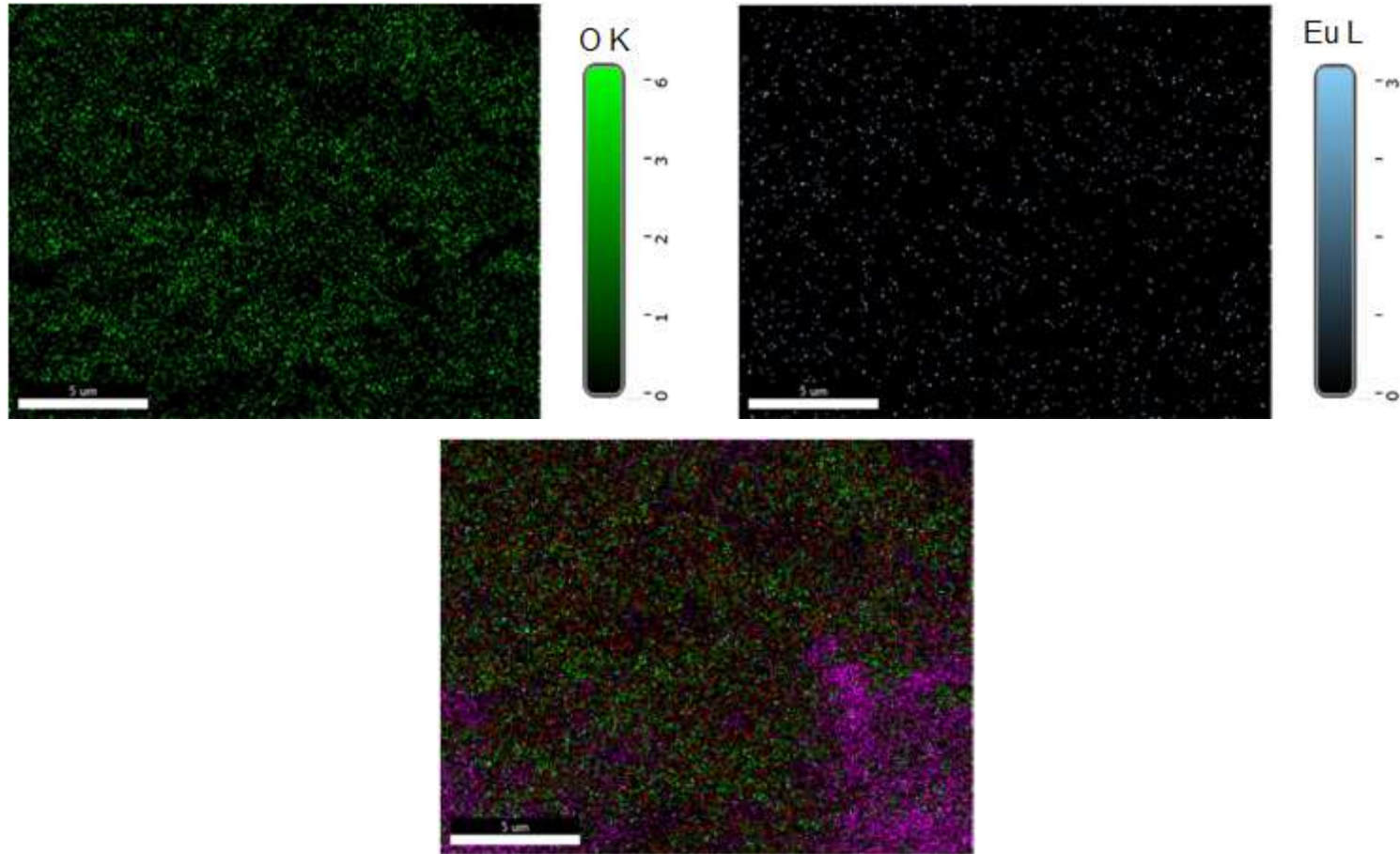
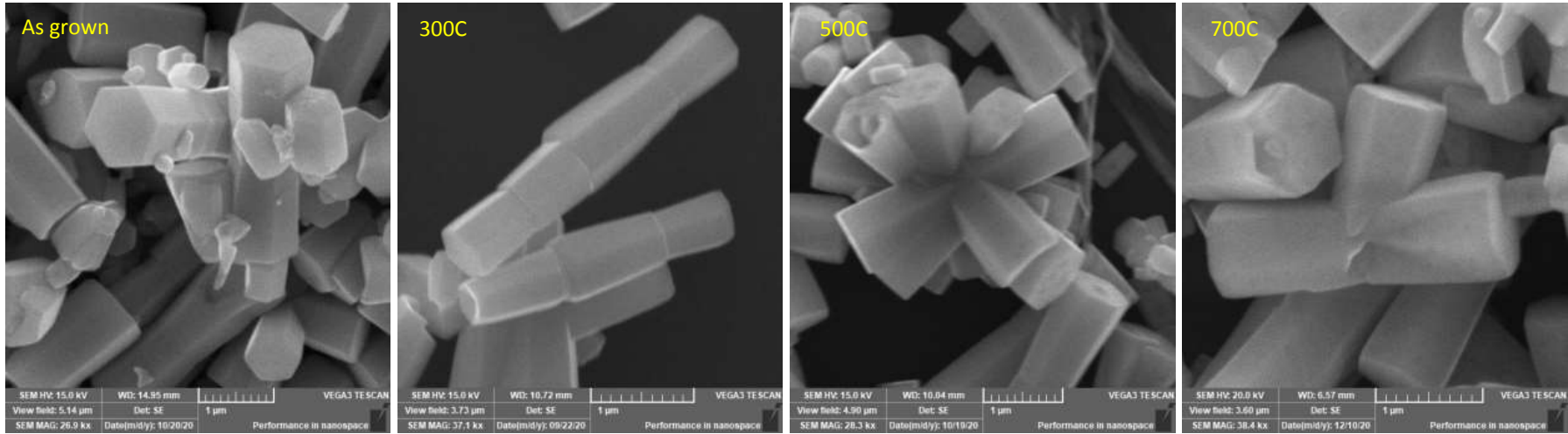
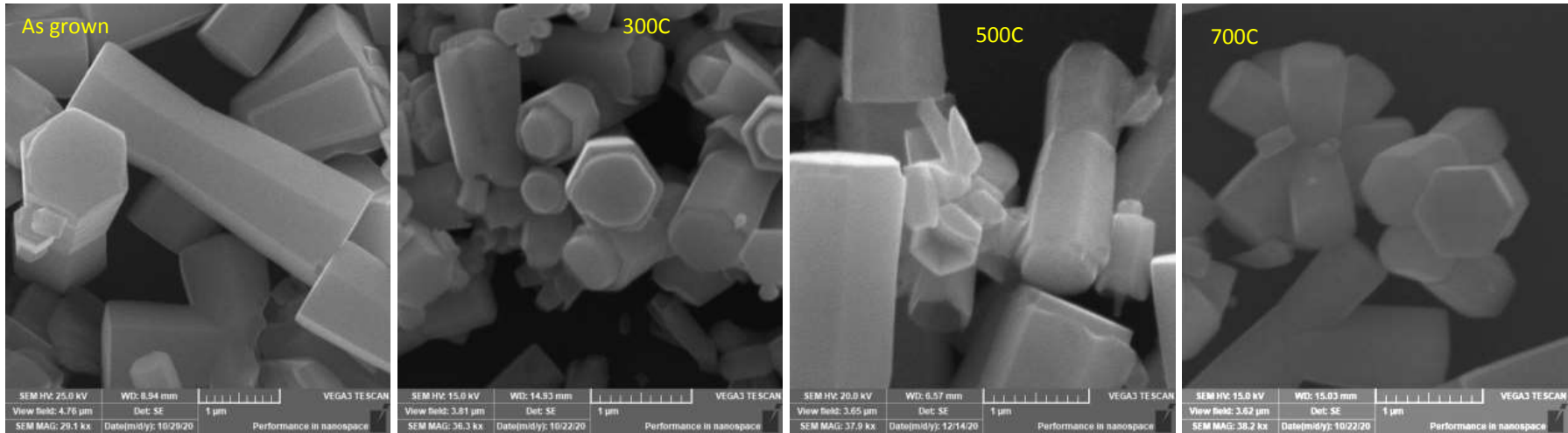


Figure 1: Element's EDX mapping and element overlap maps of 5 wt% Eu-doped ZnO as grown ($X_{\text{Eu}}=1.00\%$) (a) and that of 20 wt % Eu-doped ZnO annealed at 700 C ($X_{\text{Eu}}=2.54\%$) (b).

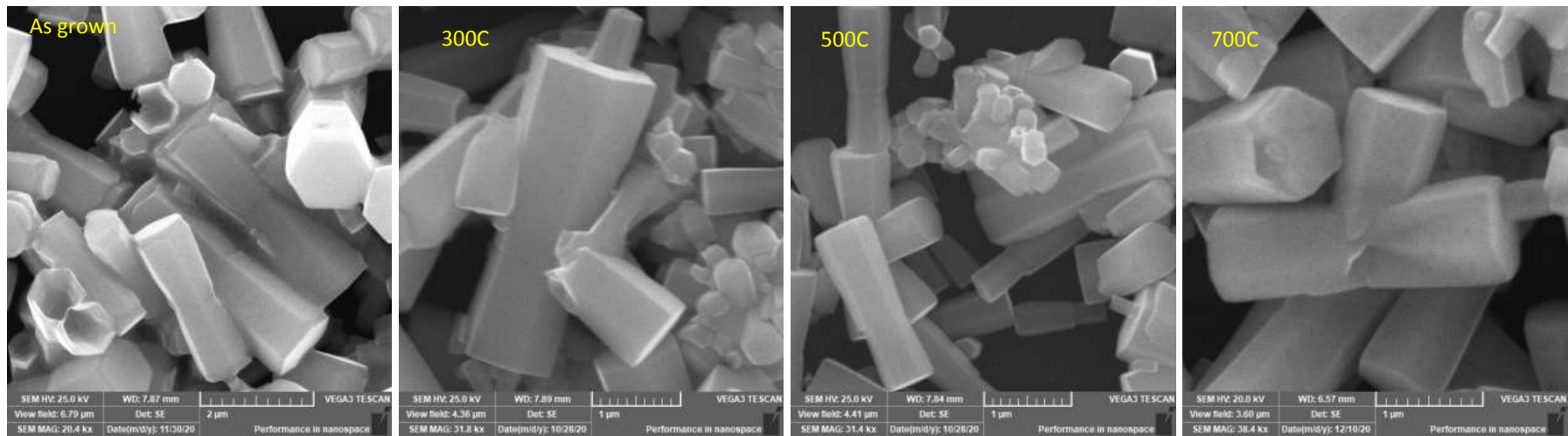
(a)



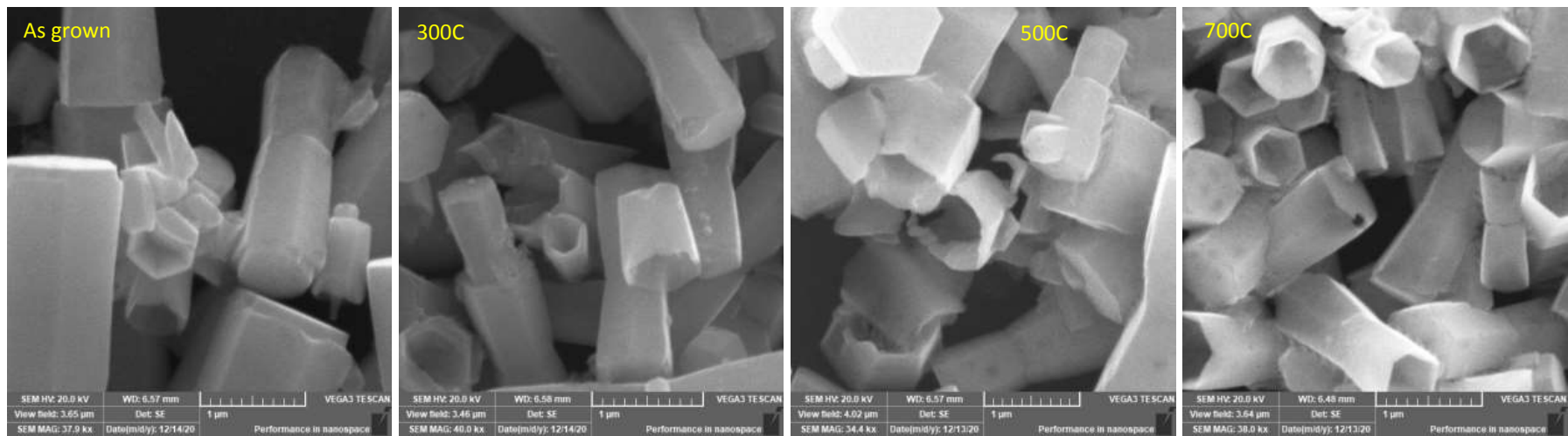
(b)



(c)



(d)



(e)

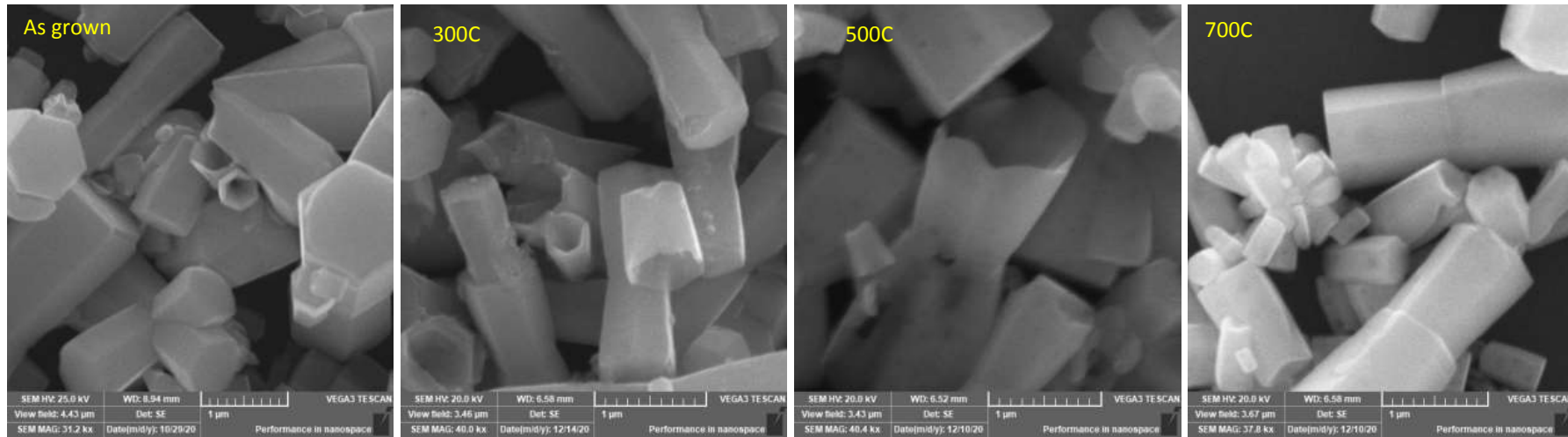
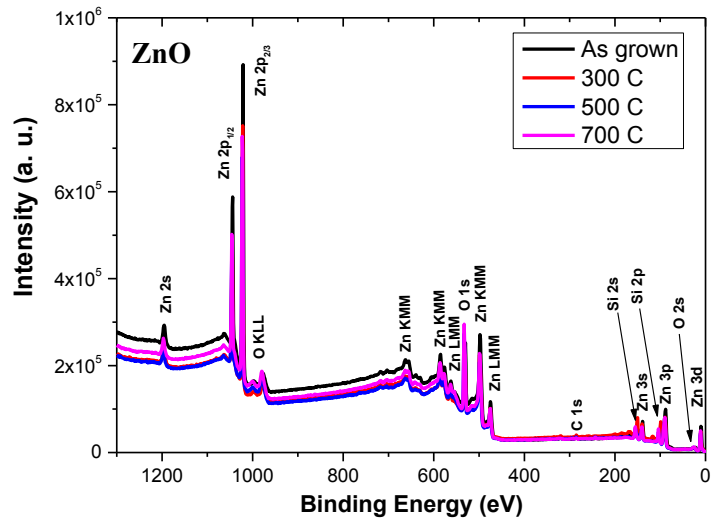
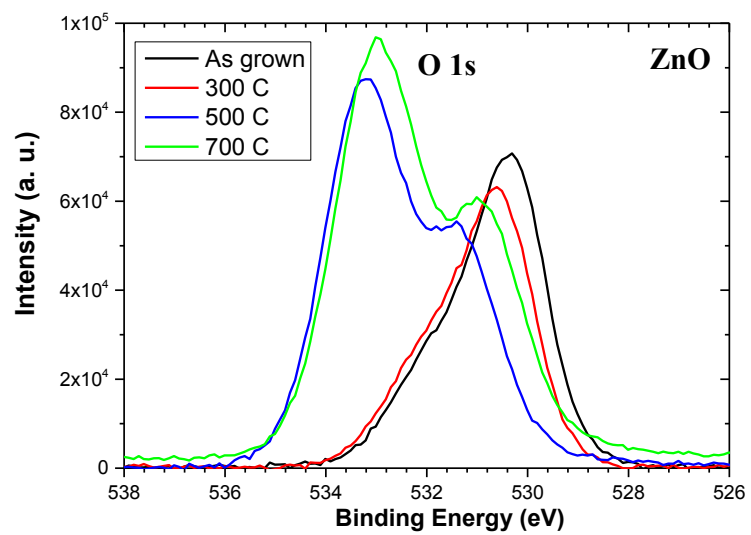
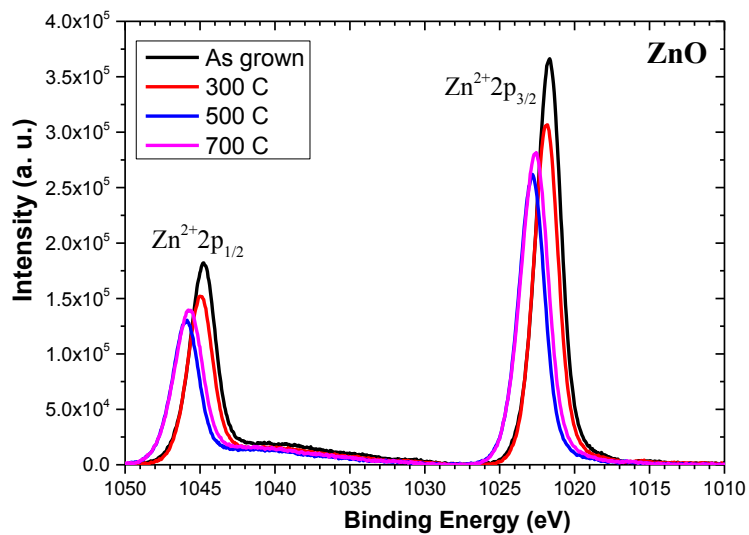


Figure 2: SEM images of (a) 0, (b) 5, (c) 10, (d) 15 and (e) 20 wt % Eu-doped ZnO micropods on p-Si substrate as grown and annealed at 300C, 500C and 700C.

(a)



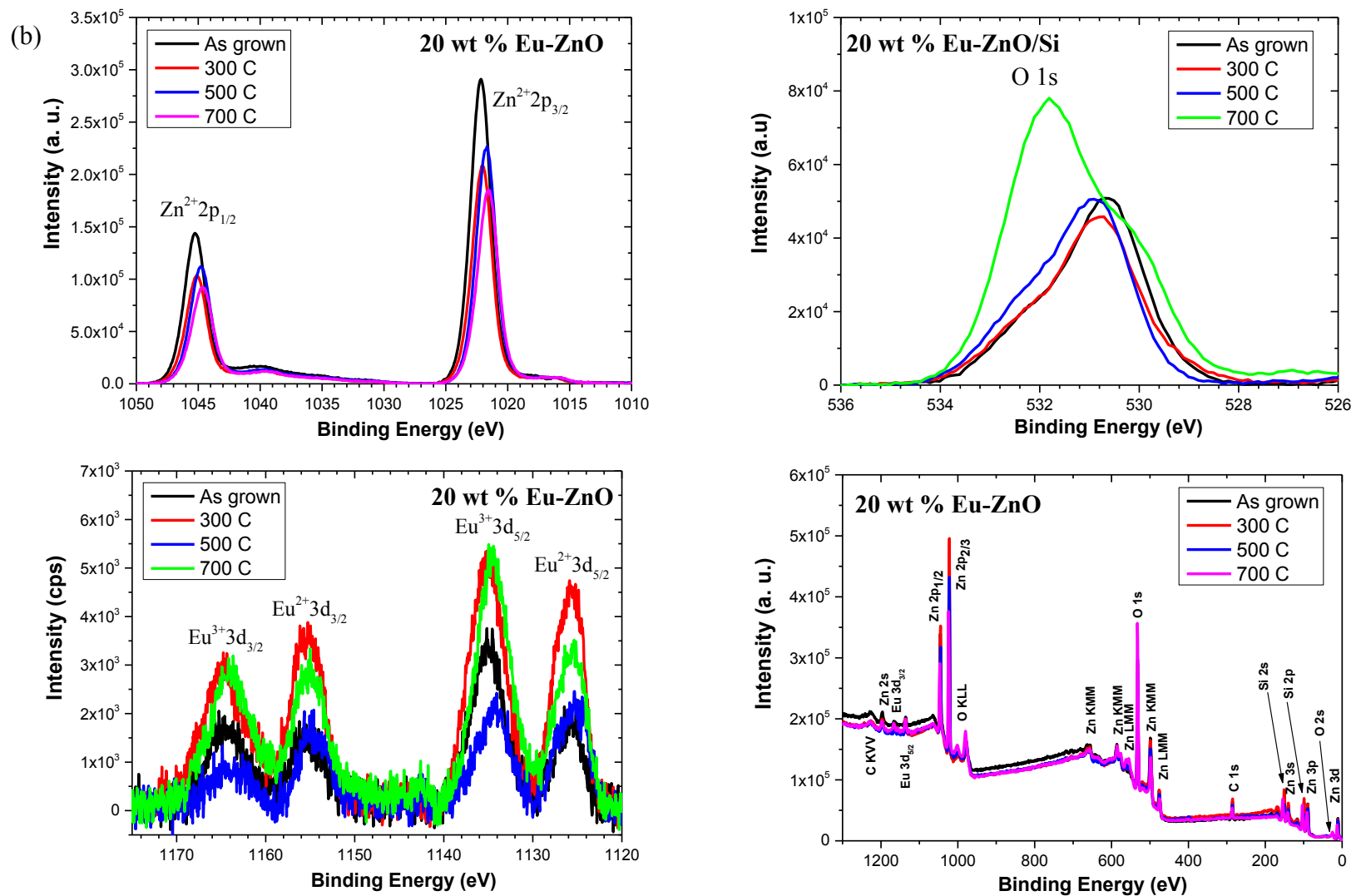


Figure 3: XPS binding energy spectra as function of annealed temperature of the (a) un-doped ZnO for Zn2p and O1s core level and (b) 20 wt % Eu-doped ZnO for Zn2p, O1s and Eu3d core level. The corresponding XPS survey spectra are also shown.

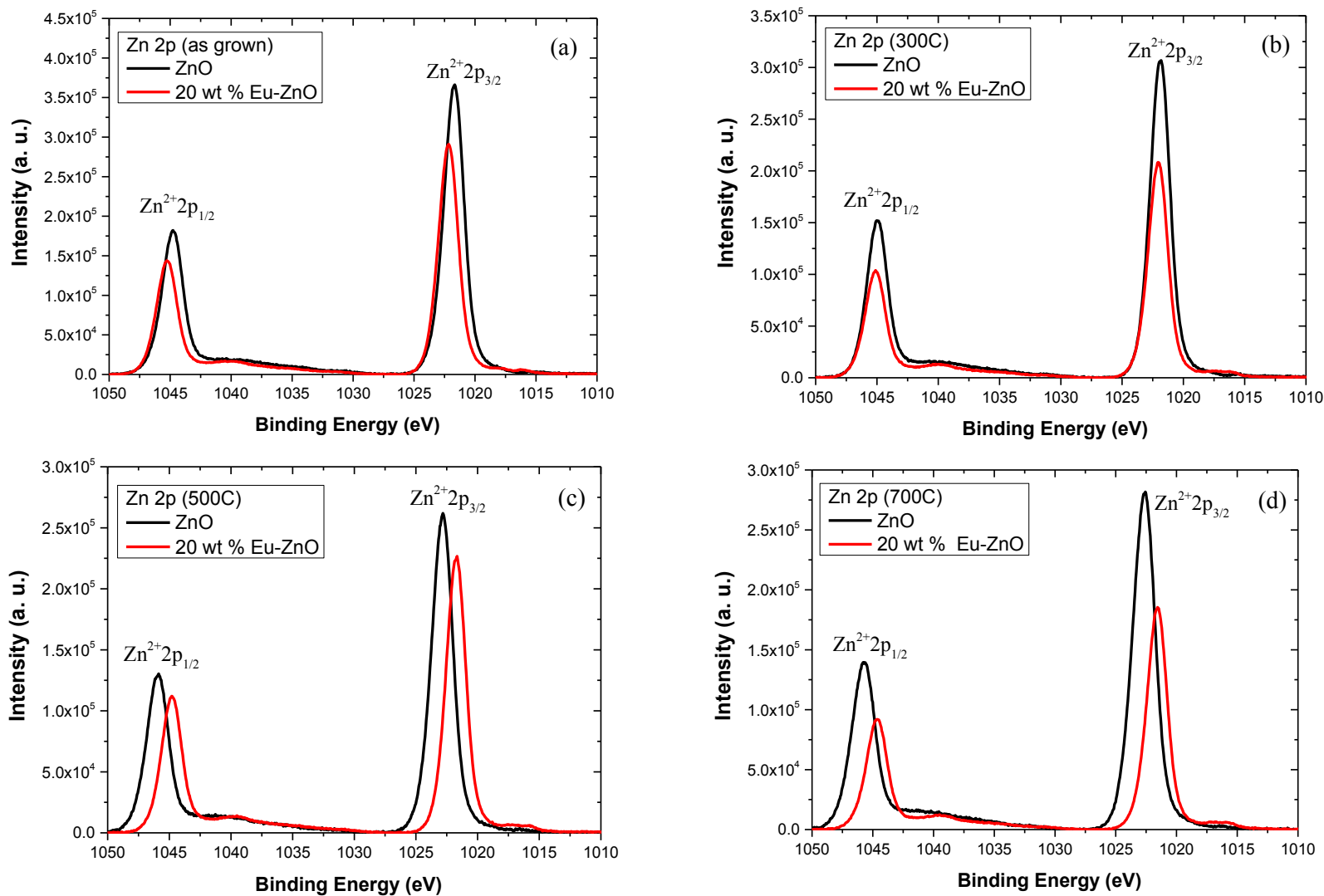
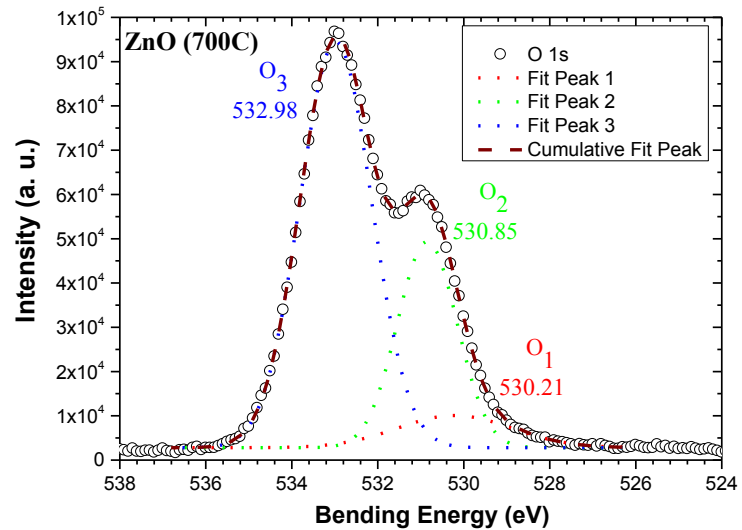
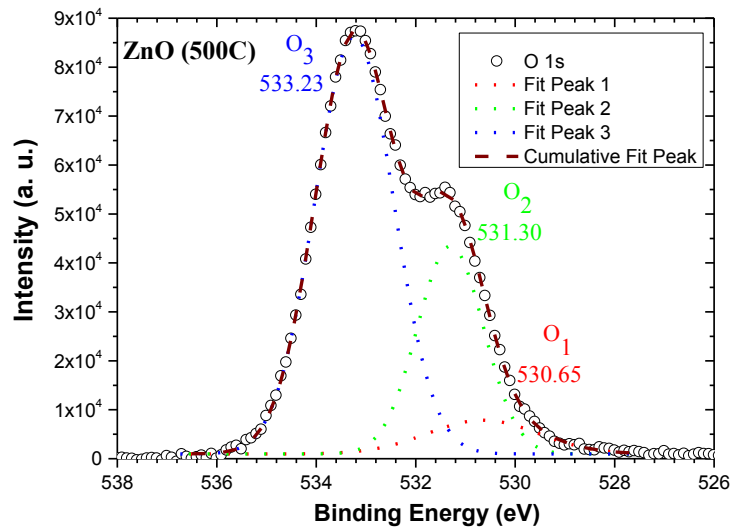
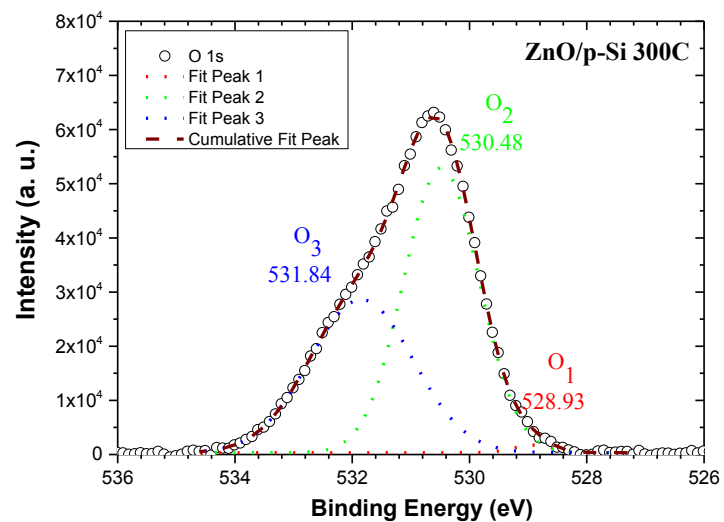
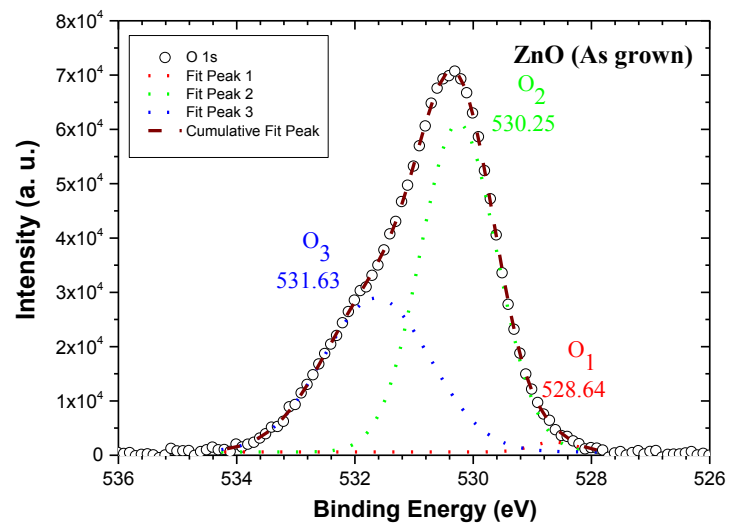


Figure 4: XPS binding energy spectra for the Zn 2p core level of un-doped and 20 wt% Eu-doped ZnO as grown (a) and annealed at 300C (b), 500C (c), 700C (d).

(a)



(b)

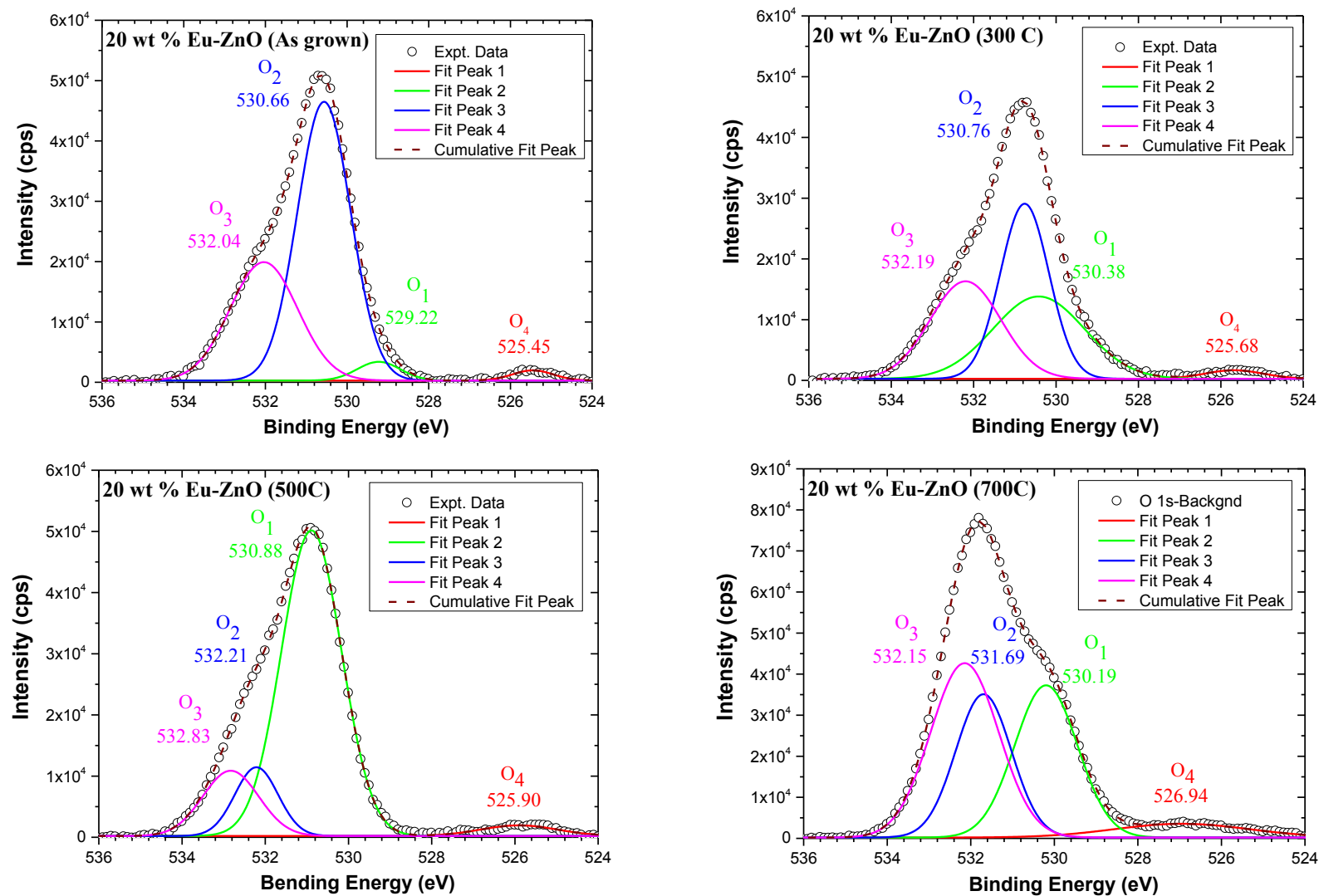


Figure 5: Deconvoluted O1s XPS core level spectra of the un-doped (a) and the 20 wt % Eu doped ZnO micropods on Si substrate (b) as grown and annealed at 300, 500 and 700C. Individual component is identified after fitting with multiple Gaussian peaks. Dashed wine line represents the cumulative fitting of all the individual peaks.

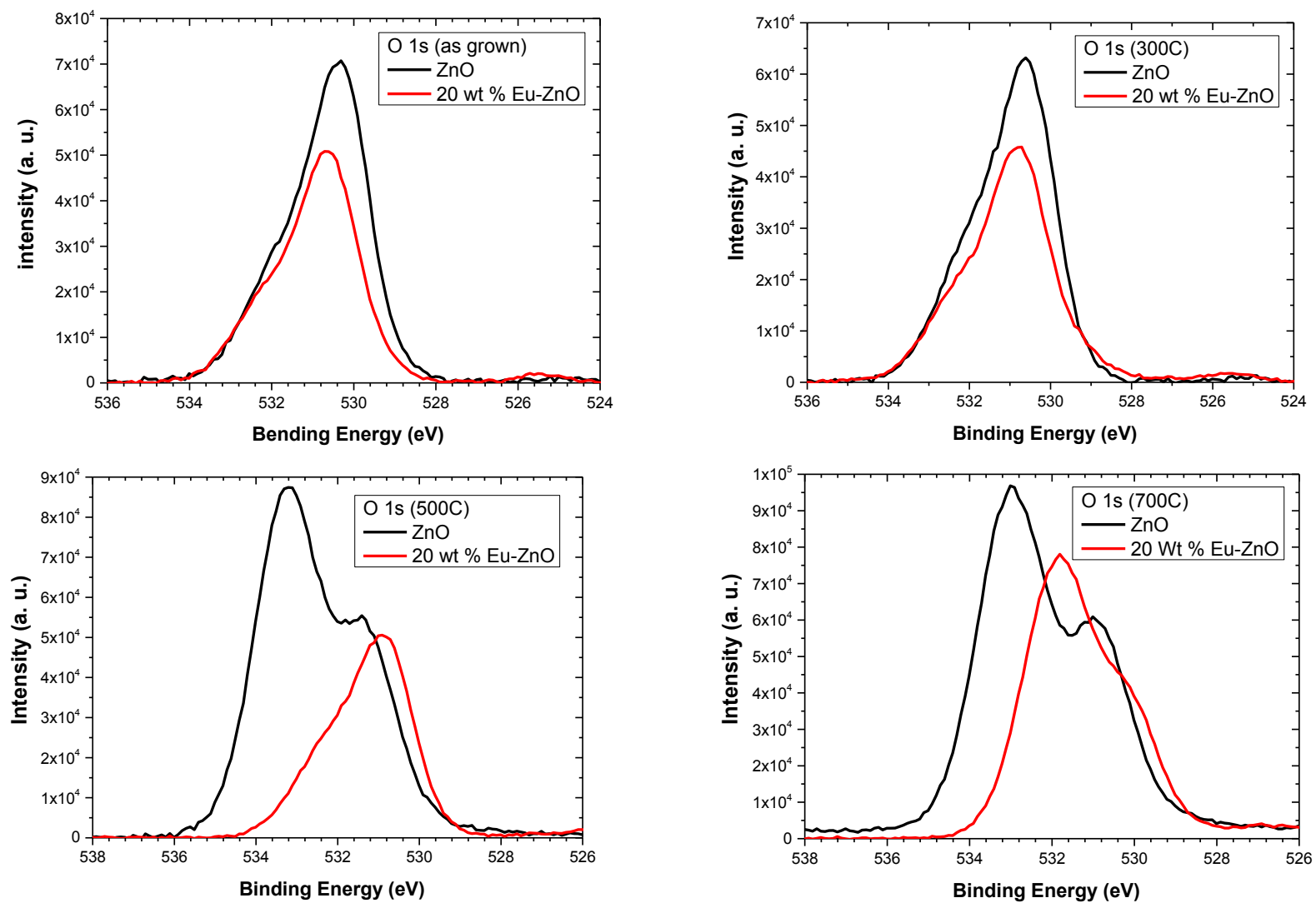
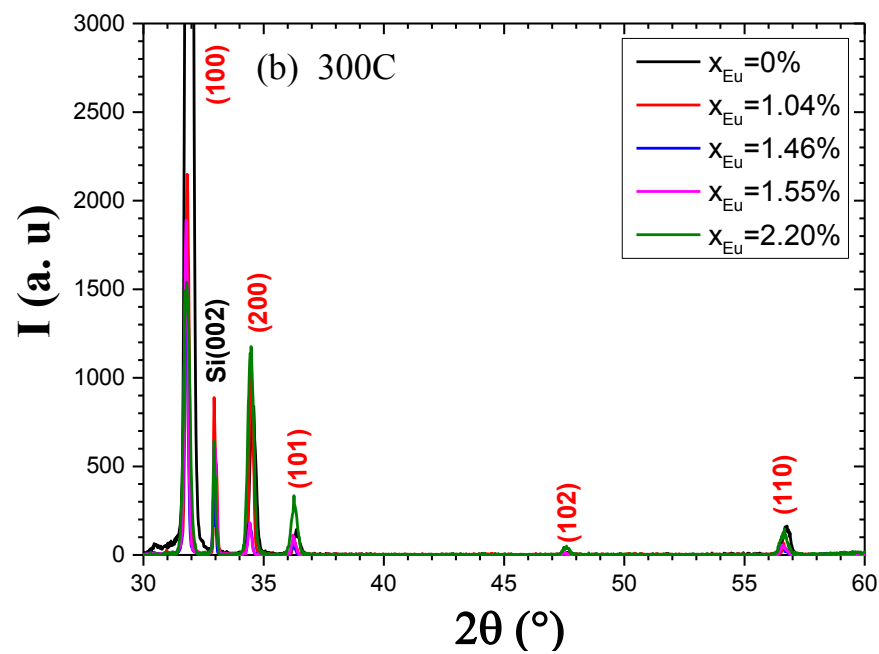
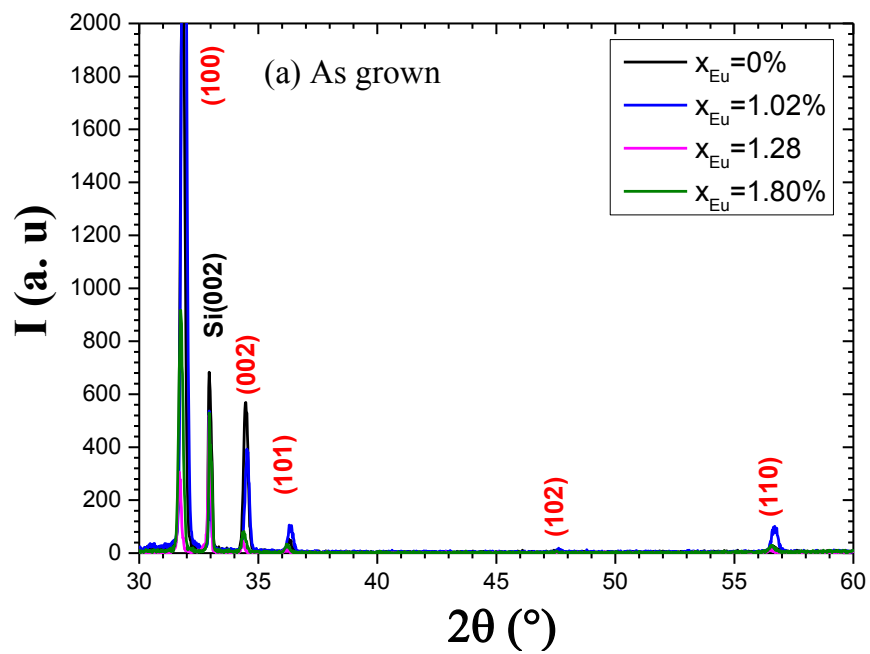


Figure 6: XPS binding energy spectra for the O 1s core level of un-doped and 20 wt % Eu-doped ZnO micropods annealed at the same temperature.



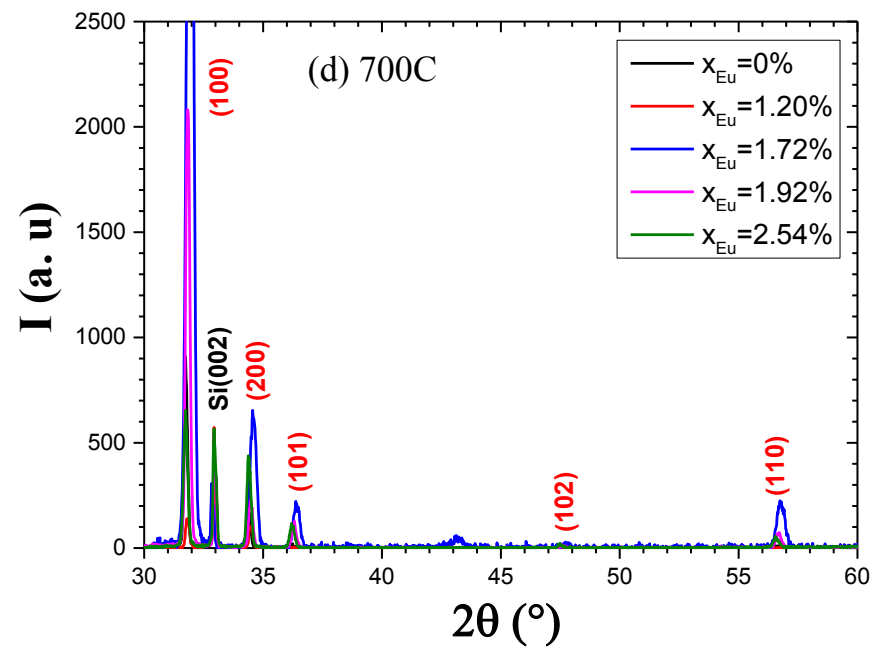
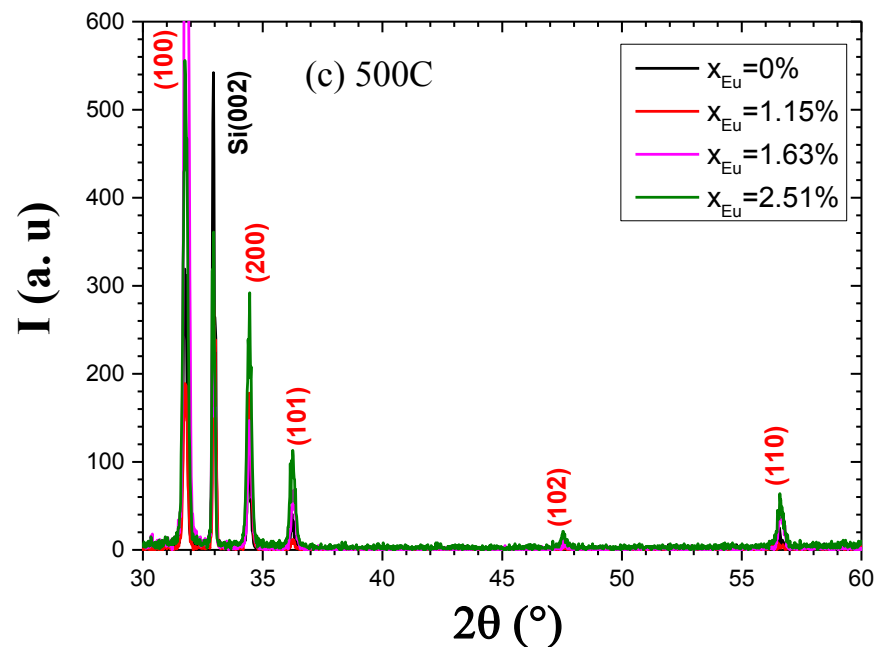
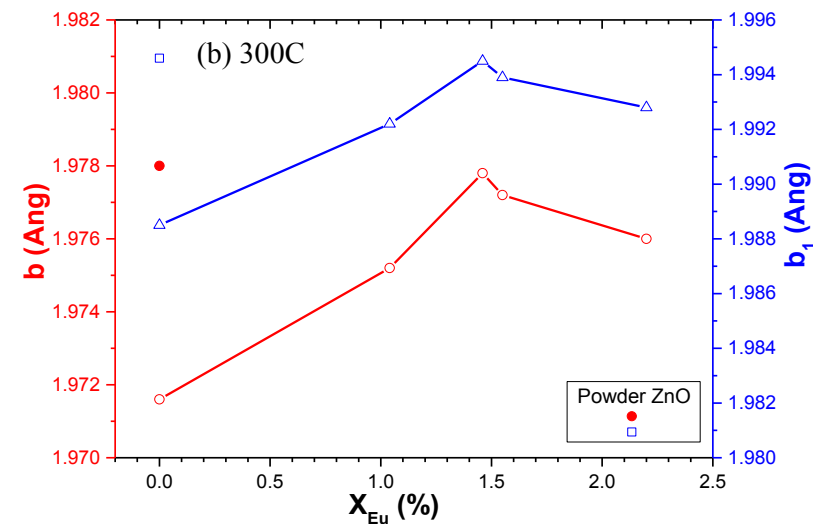
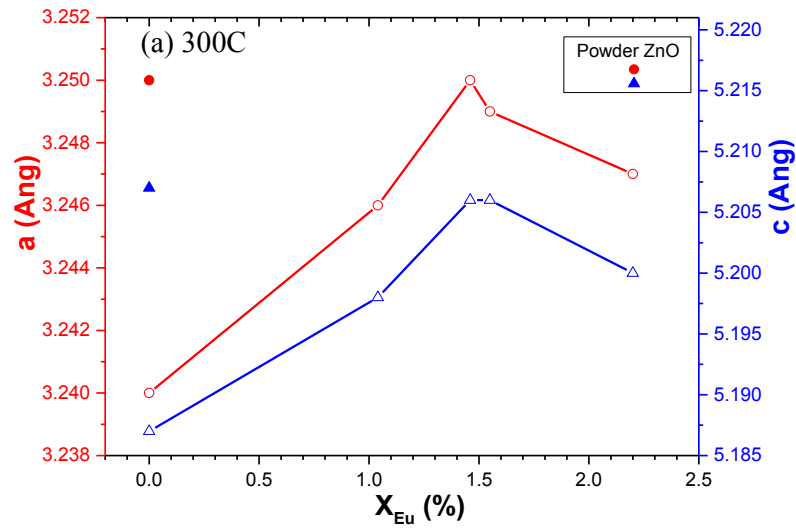
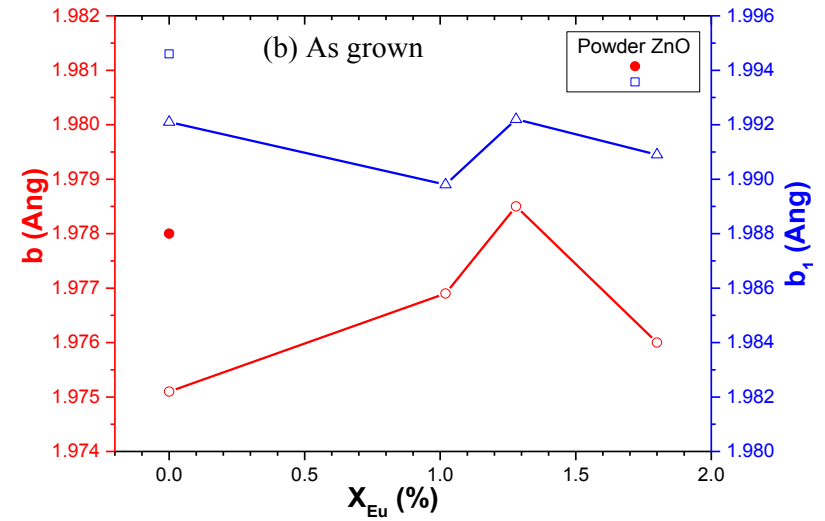
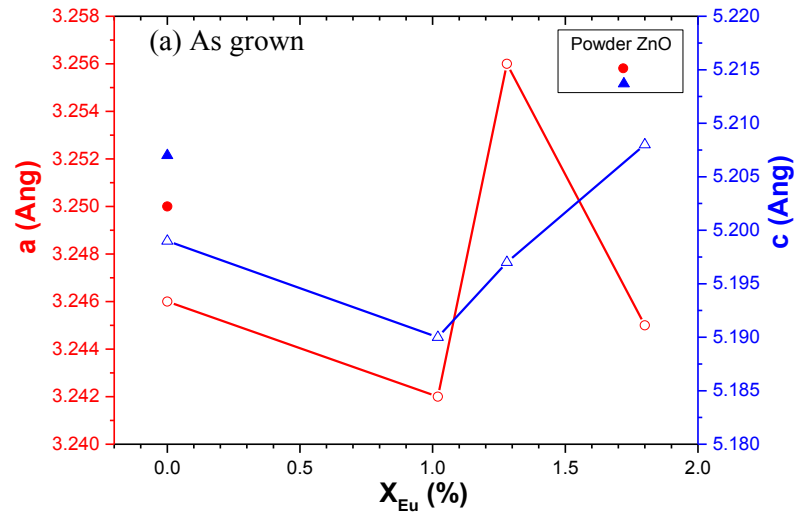


Figure 7: X-ray diffraction spectra of X% Eu doped ZnO micropods on p-Si substrate as grown (a), annealed respectively at 300 C (b), 500C (c), and 700C (d).



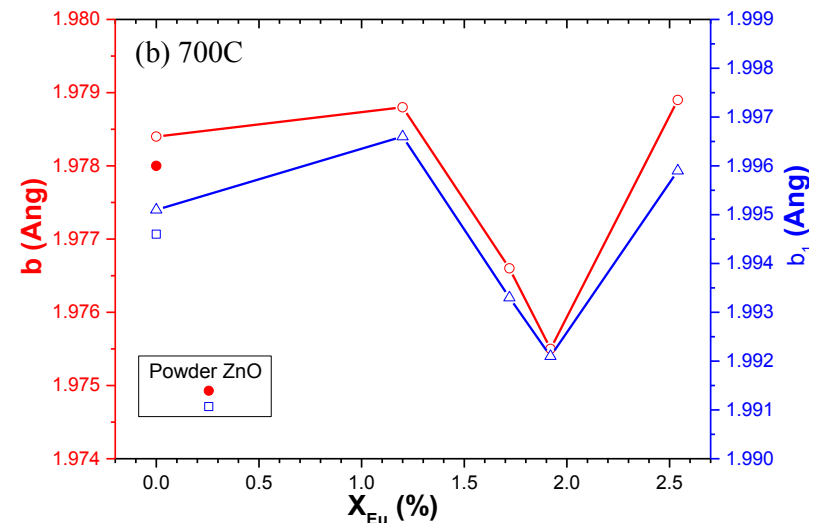
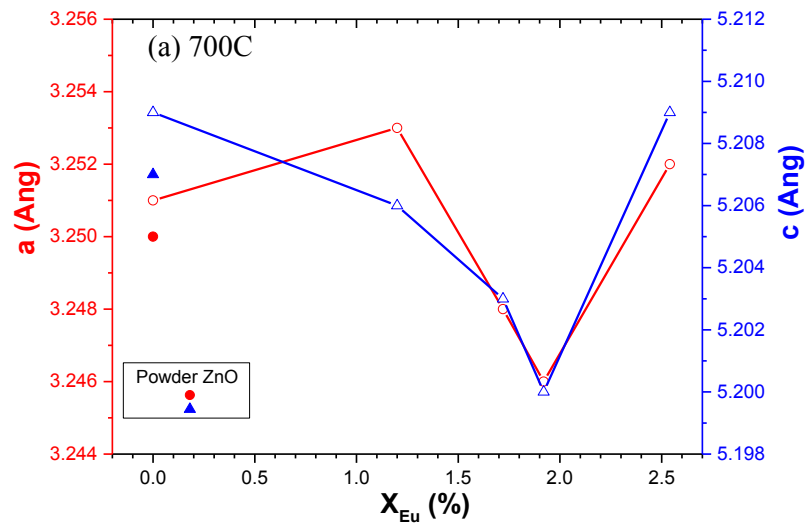
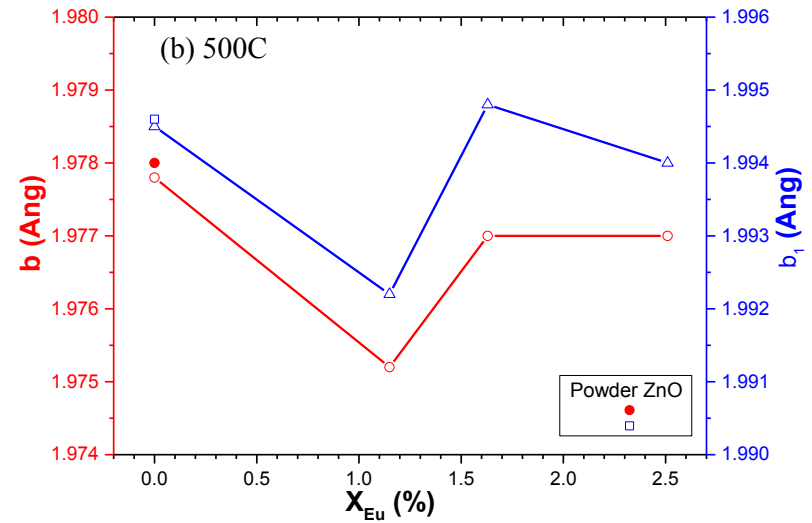
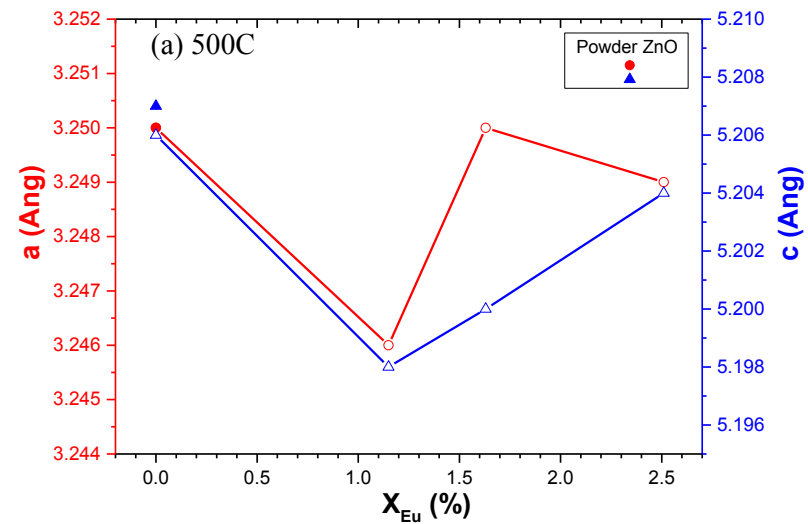


Figure 8: Variation of (a) lattice parameters and (b) the bond length b and b_1 with the europium concentration incorporated and for the different annealed temperature.

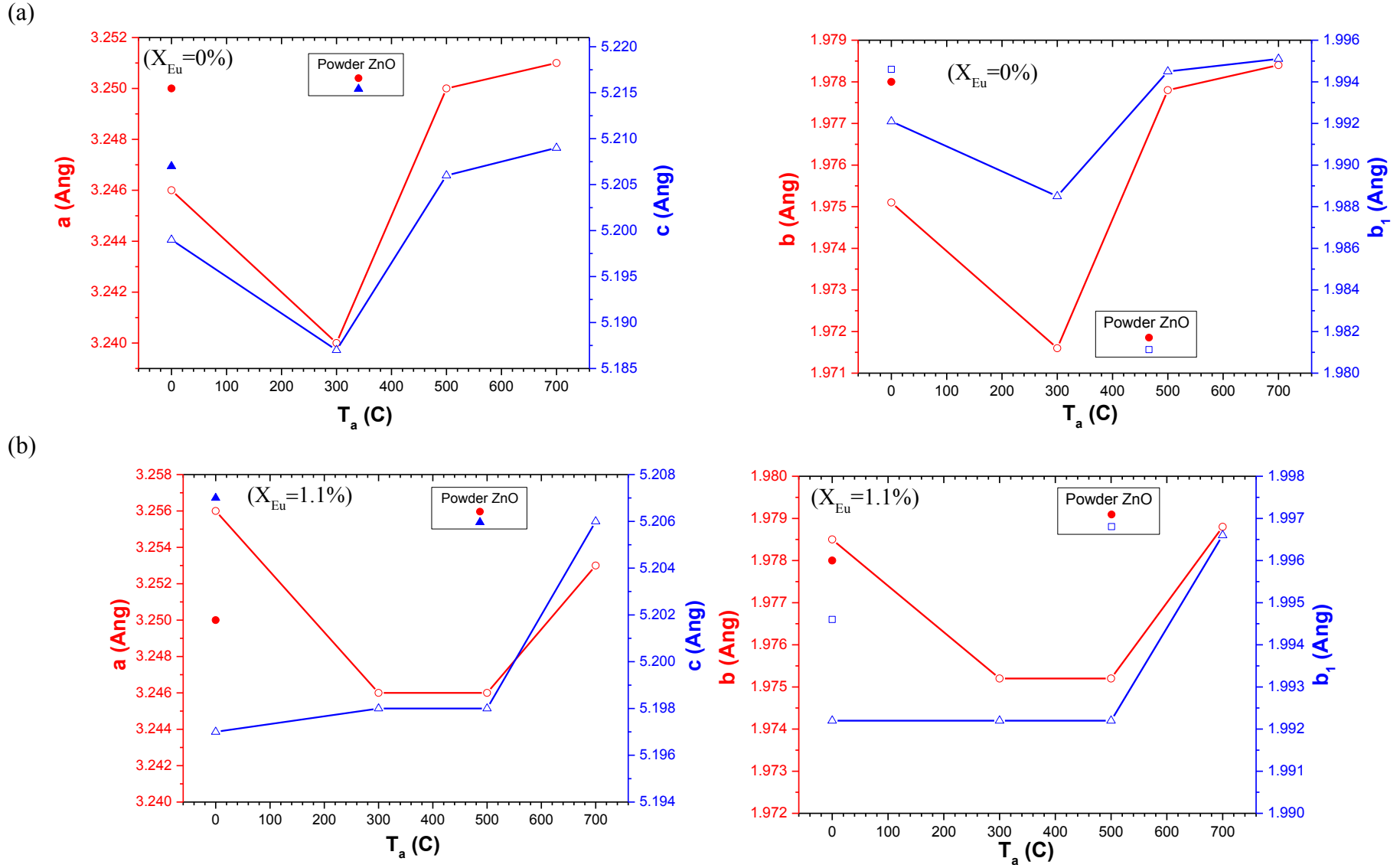


Figure 9: Variation of lattice parameters and bond length for (a) un-doped and (b) doped ($X_{Eu} \approx 1.1\%$) ZnO micropods with annealing temperature T_a .

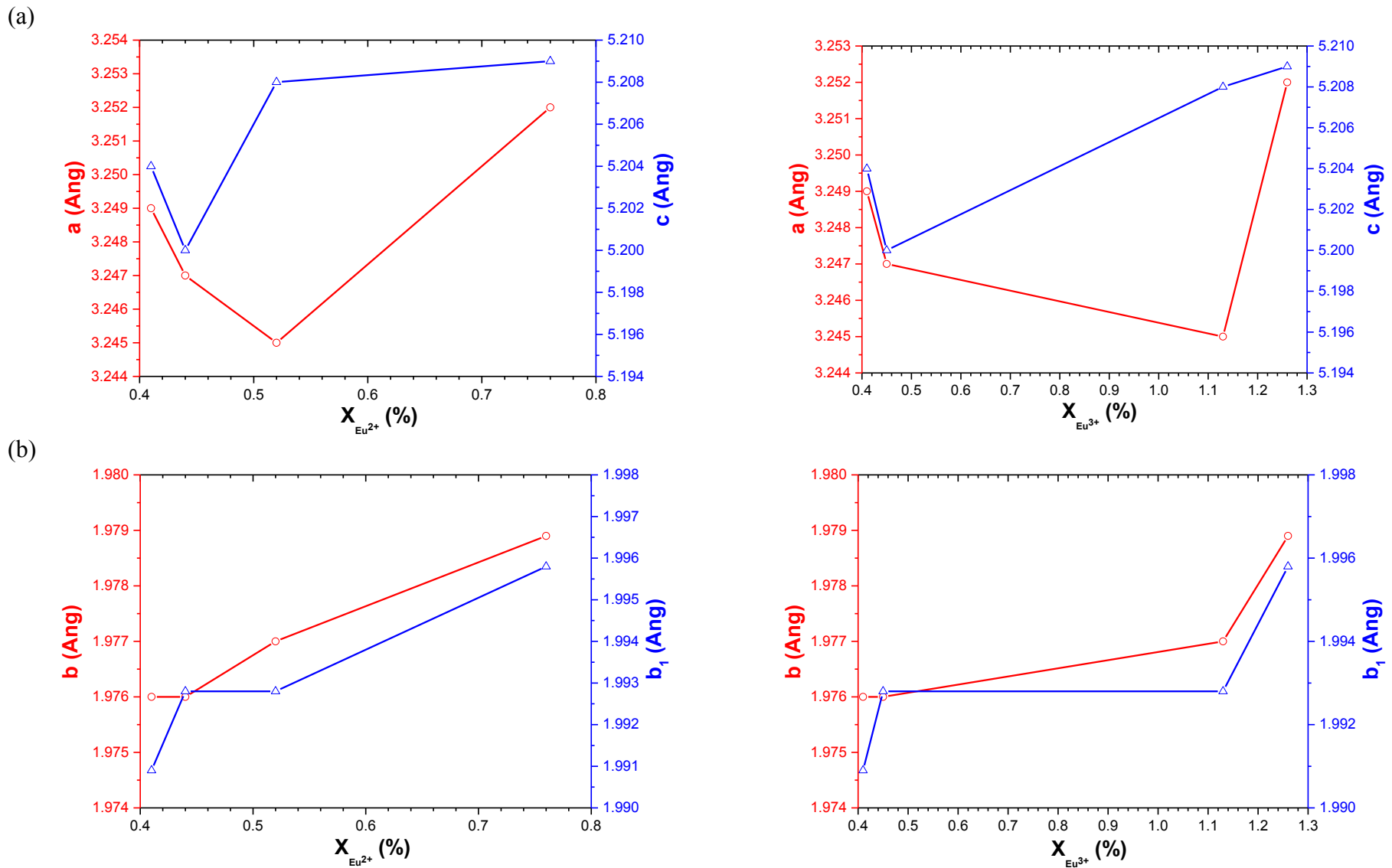


Figure 10: Variation of lattice parameters (a) and bond length (b) with Eu²⁺ and Eu³⁺ concentration for sample 20 wt% Eu doped ZnO micropods annealed at different temperature.

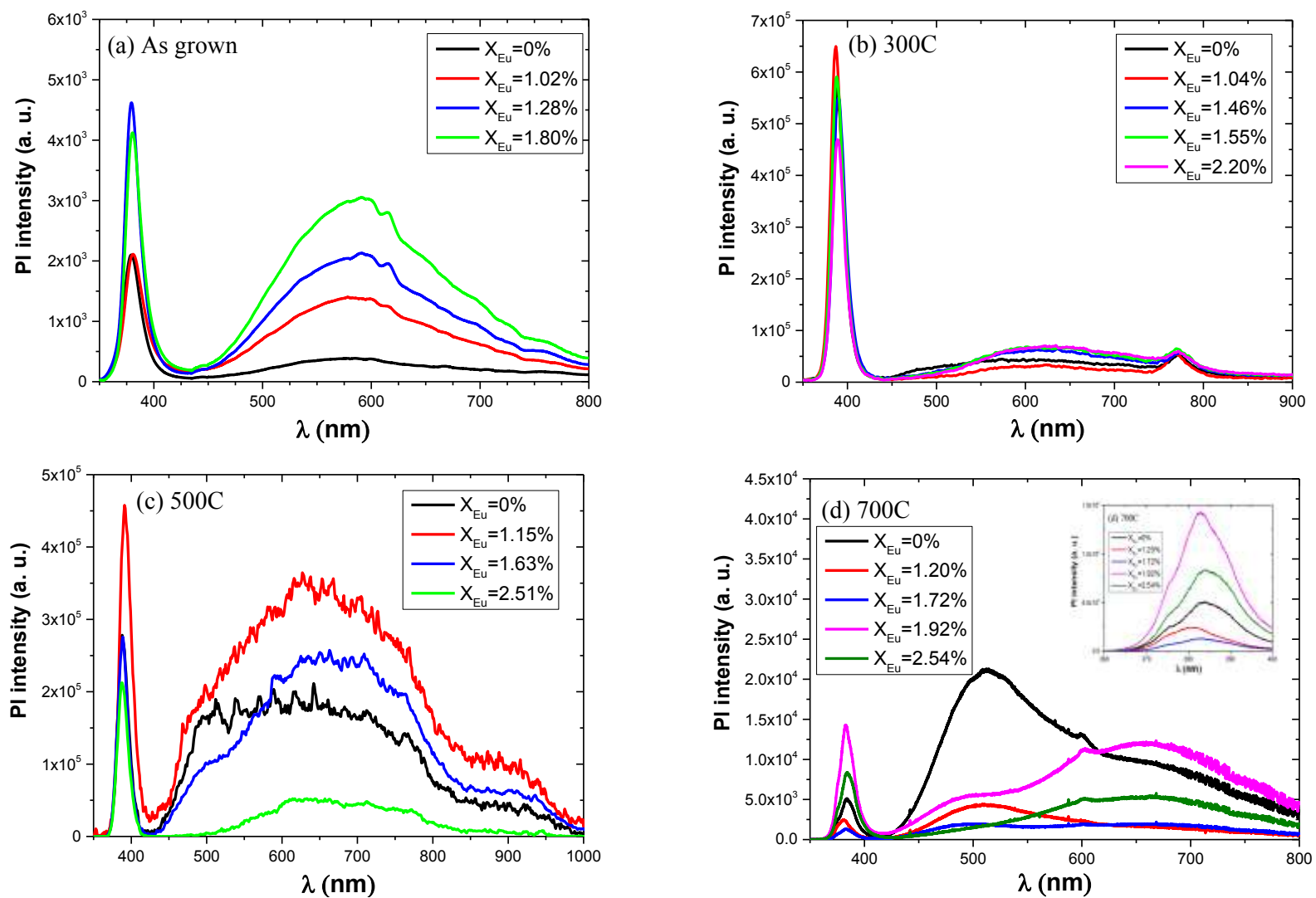


Figure 11: Photoluminescence spectra (excited at 325 nm) of Eu doped ZnO micropods on p-Si substrate as grown (a), annealed respectively at 300 C (b), 500C (c) and 700C.

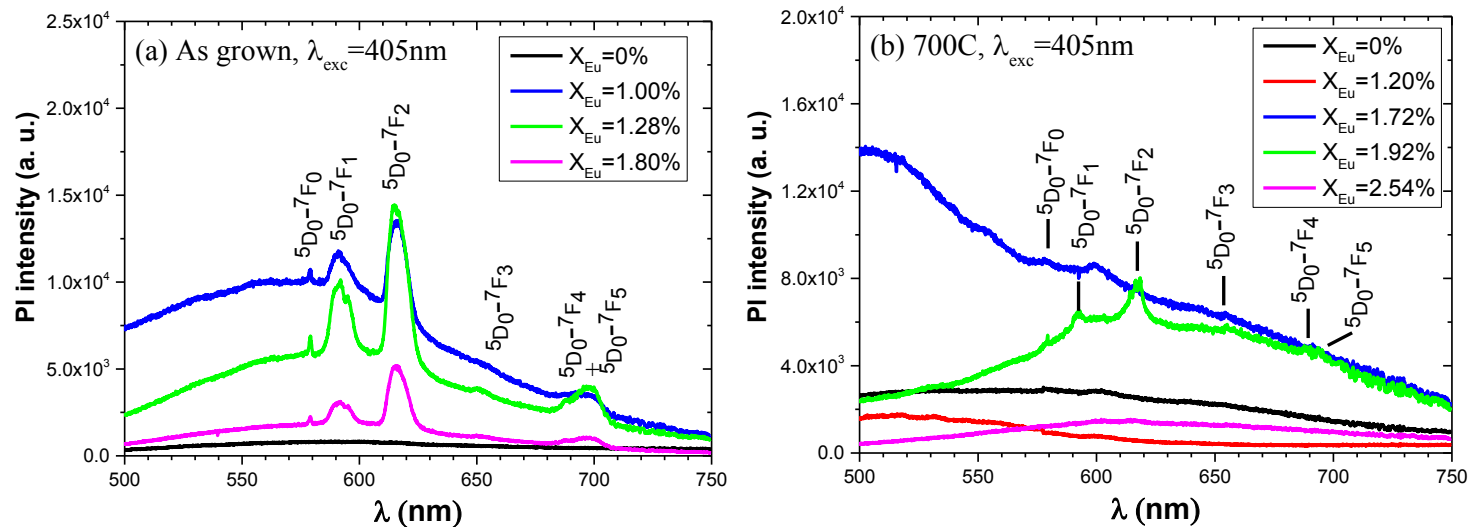


Figure 12: Photoluminescence spectra (excited at 405 nm) of Eu doped ZnO micropods on p-Si substrate (a) as grown (b) and annealed at 700 C.

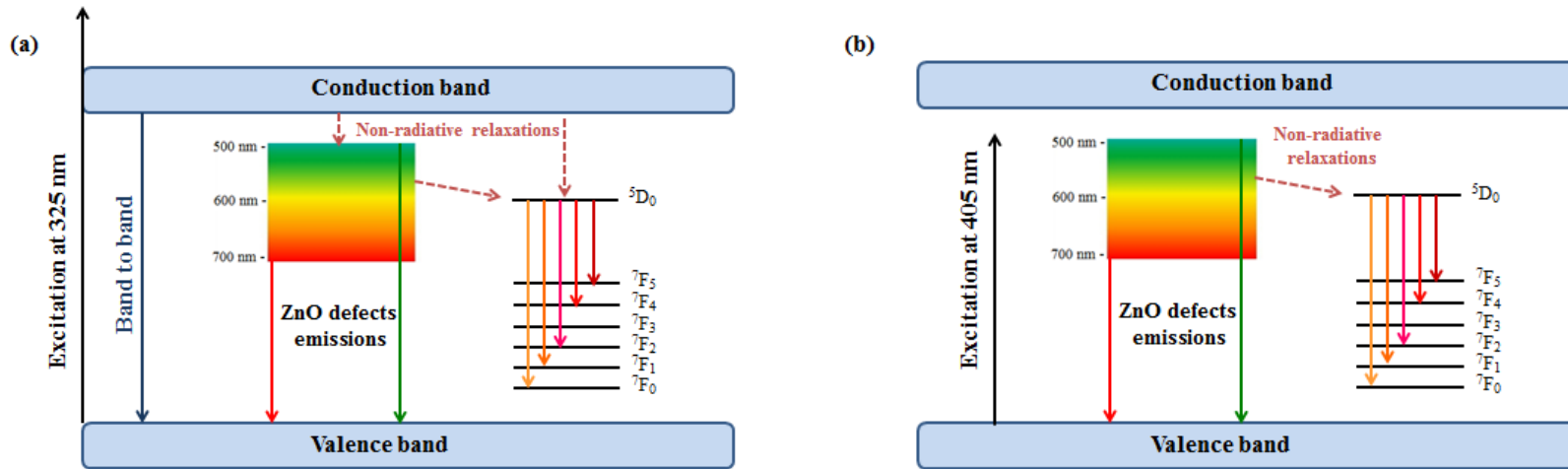


Figure 13: Eu-doped ZnO schematic energy level diagram illustrating ZnO and Eu^{3+} ion emissions and the energy transfer mechanism between them when excited at wavelengths of (a) 325 and (b) 405 nm.

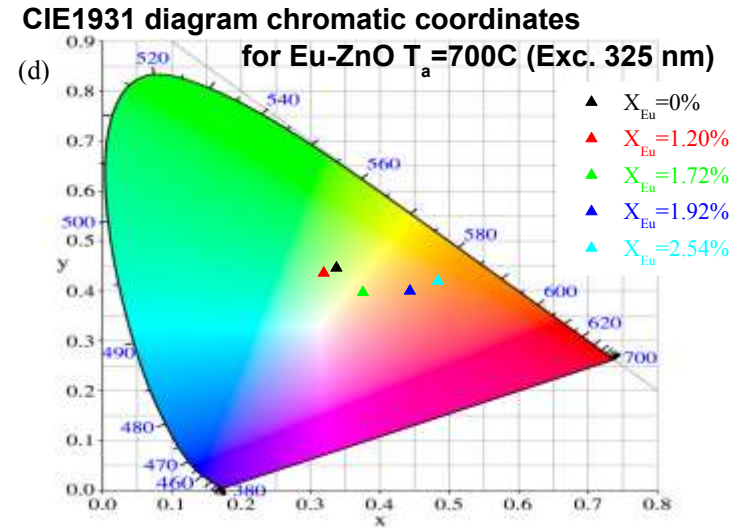
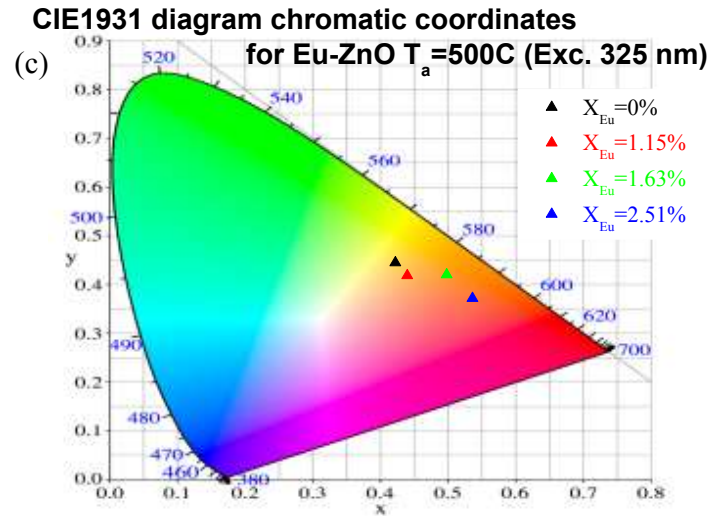
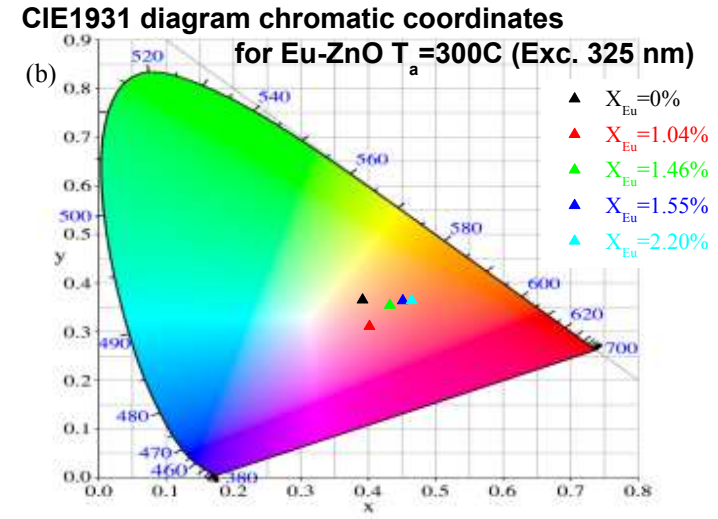
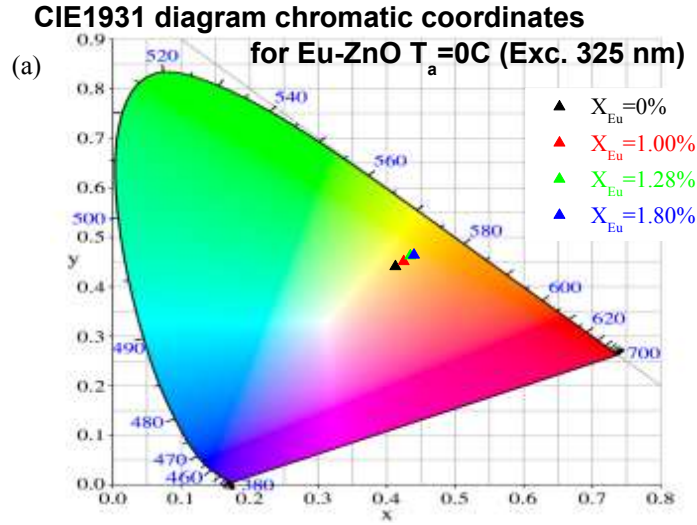


Figure 14: CIE coordinates diagram ($\lambda_{\text{exc}}=325\text{ nm}$) of un-doped and Eu-doped ZnO samples as grown (a) and annealed at 300 C (b), 500 C (c) and 700C (d).

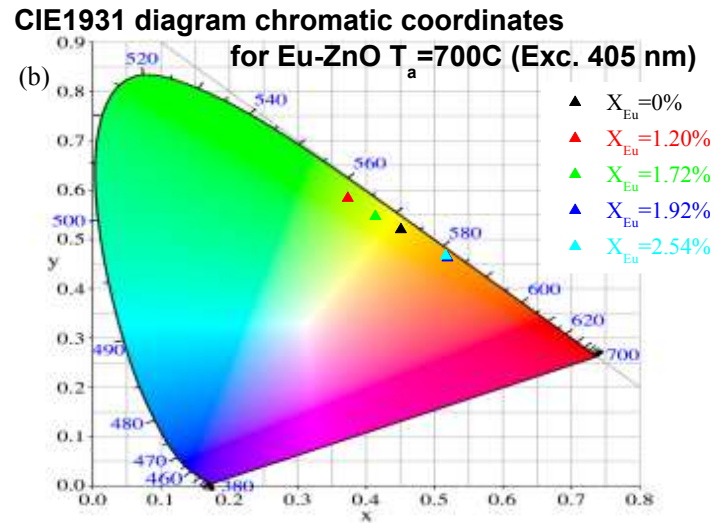
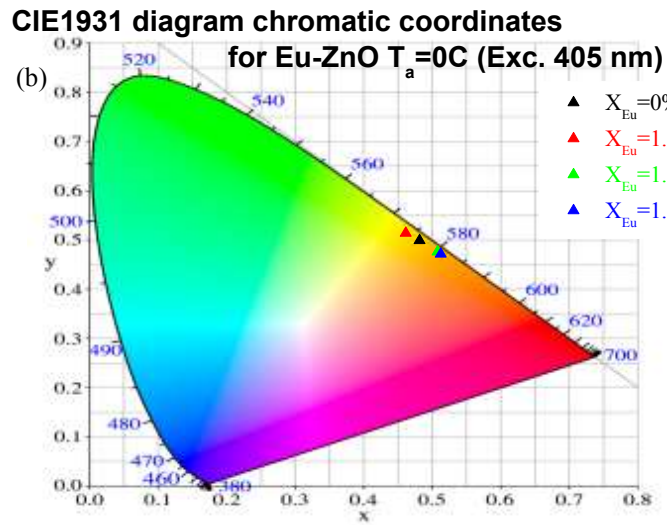


Figure 15: CIE coordinates diagram ($\lambda_{exc}=405\text{ nm}$) of un-doped and Eu-doped ZnO samples as grown (a) and annealed at 700C (d).

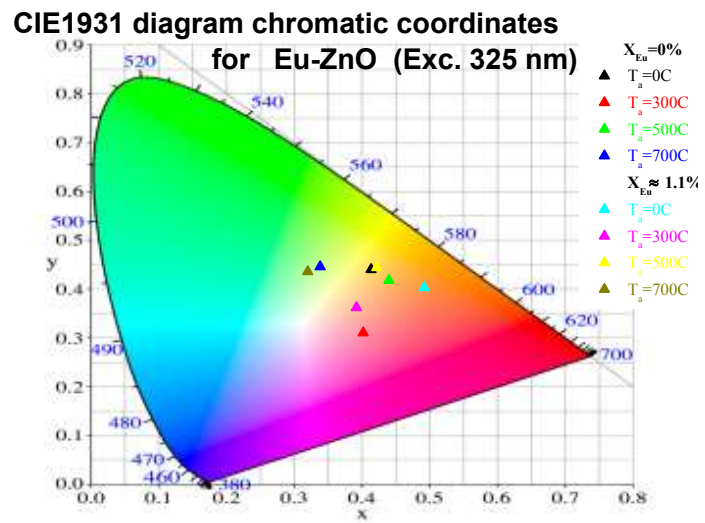


Figure 16: CIE coordinates diagram ($\lambda_{exc}=325$ nm) of un-doped and $\approx 1.1\%$ Eu-doped ZnO micropods for different annealing temperature.

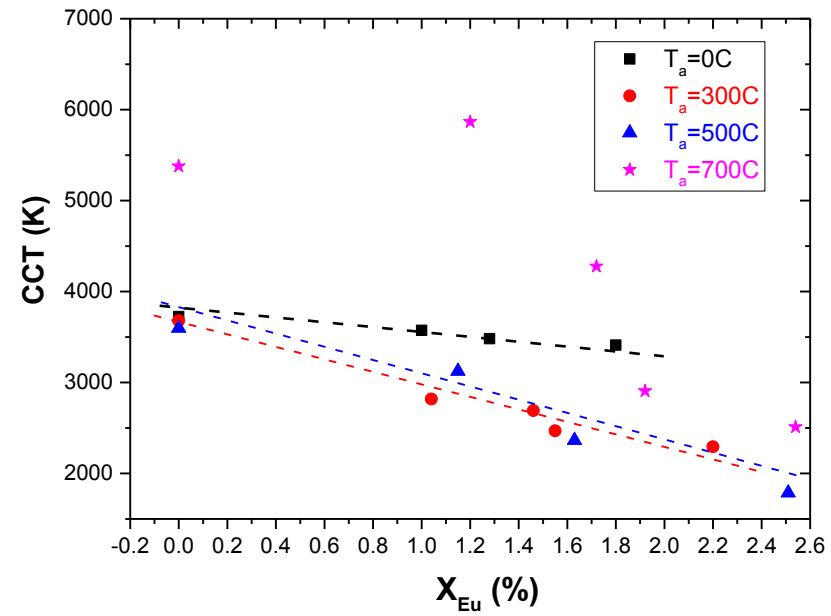


Figure 17: CCT ($\lambda_{exc}=325$ nm) of Eu-doped ZnO micropods as function of Eu concentration for different annealing temperature.

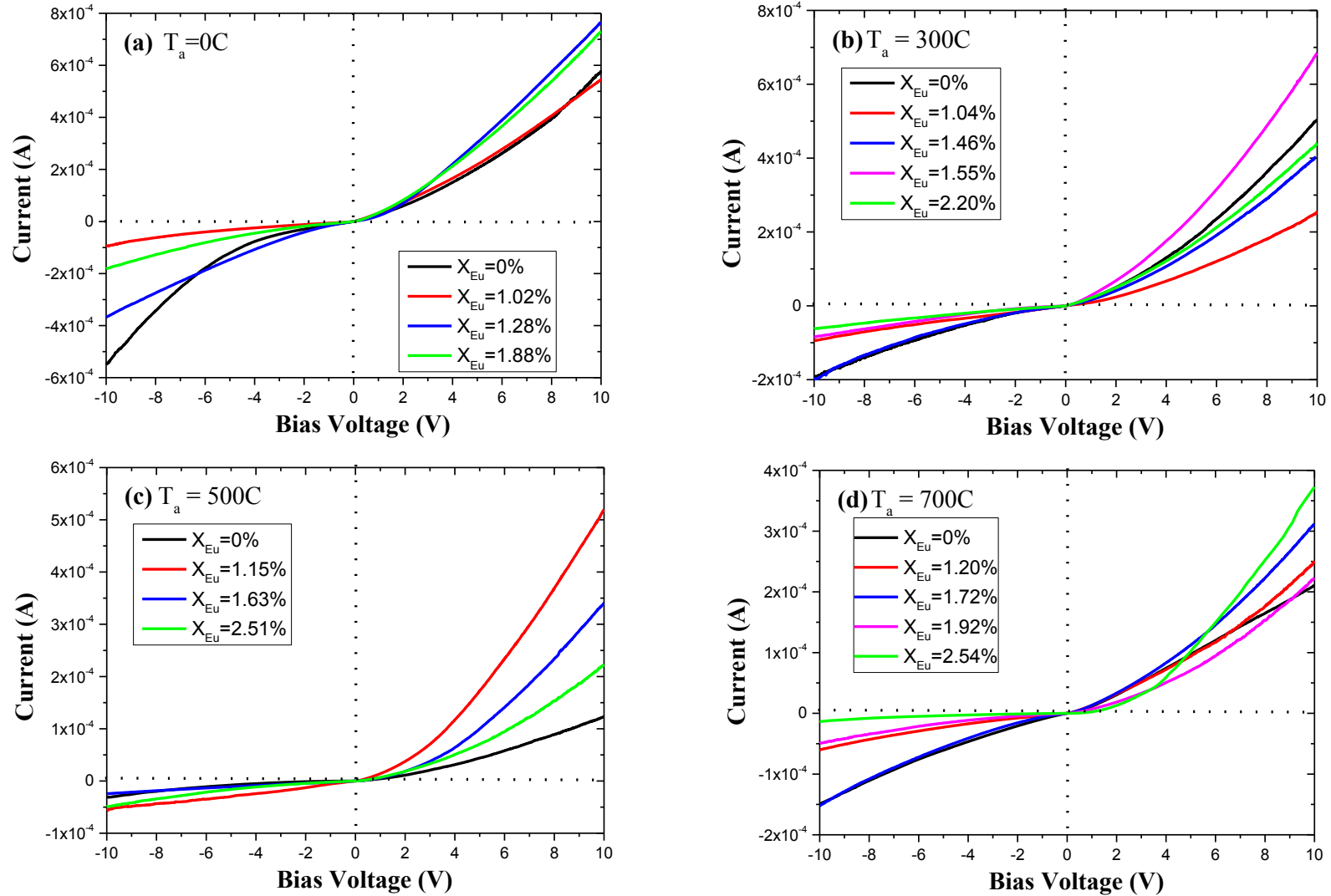


Figure 18: Plots of the current–voltage ($I-V$) characteristics of Eu doped ZnO micropods on p-Si substrate for the different europium concentration incorporated (a) as grown and annealed for 2 hours at (b) 300C , (c) 500C, and (d) 700C.

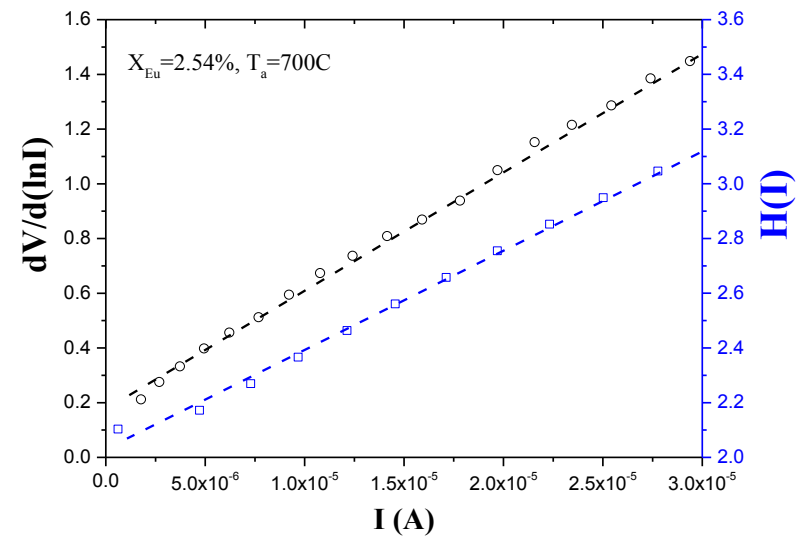
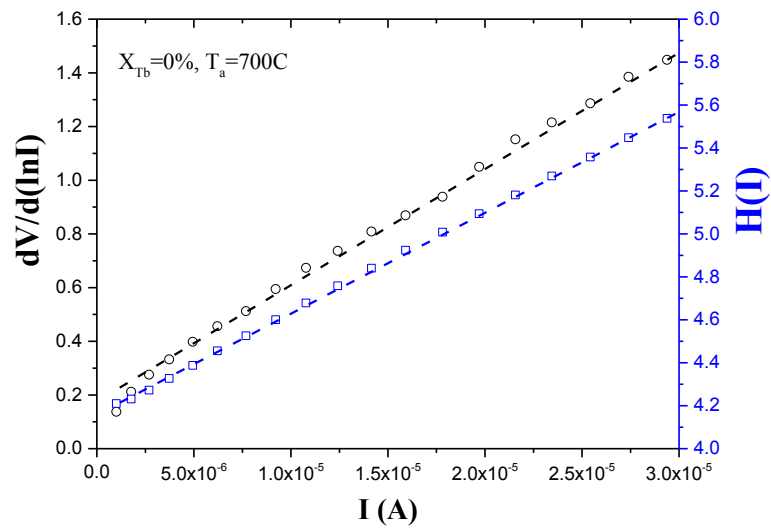


Figure 19: $dV/d(\ln I)$ - I and $H(I)$ - I plots of un- and 2.54% Eu doped heterojunction sample annealed at 700C.